

MEASUREMENT OF RABI OSCILLATION IN A SPIN SYSTEM

by

Jordan Lovis, H.BSc.

A thesis submitted to the Faculty of Graduate Studies in partial fulfillment
of the requirements for the degree of Masters of Science in Physics

Department of Physics
Lakehead University

August 2018

ABSTRACT

This work proposes that during the application of an on-resonance MR-pulse there exists a Rabi oscillating field which can be directly measured from a nuclear spin system. These oscillations have been previously inferred through a series of varied pulsed-length free induction decay (FID) measurements, however direct observation of a continuous oscillation has not previously been reported. Due to the existence of this oscillation only during application of an radio-frequency (RF) field, it's detection is complicated by the strength of the applied RF which is orders of magnitude greater than Rabi signal. In order to mitigate the overpowering signal from the applied RF field, several signal conditioning stages were required for detection of these oscillations. The dependency of the detected Rabi oscillation frequency with respect to strength of the applied RF field, and sample size were validated. Furthermore, the field strength due the observed Rabi oscillations was determined and compared to theoretical simulations to within experimental accuracy.

ACKNOWLEDGEMENTS

Although one name is written on the title page of this thesis, the work presented is in reality the result of the combined efforts of a number of people, to all of whom, I owe a great deal.

Firstly, I would like to thank my supervisor Dr. Patrick Rapley whose support, advice, ideas, and accessibility has been invaluable to me through my time here spent at Lakehead University.

I am indebted to Dr. Werden Keeler whose mentorship and professional support through the course of this work I will be forever grateful for. Without his insight and expertise in advanced circuitry the completion of this work would not be made possible.

Many thanks must go to Mr. Yuri Shepelytskyi who's technical support in pulse sequence design proved to be invaluable.

I would like to thank the remaining members of my advisory committee, Dr. Appichart Linhananta, and Dr. Peter McGhee both of whom provided guidance and mentorship throughout my time at Lakehead.

Continuing on a professional level, I would like to thank all the technical staff at both Thunder Bay Regional Health Sciences Centre and Lakehead University whose expertise and advice lead to the completion of this work: Ms. Kendra Rys, Mr. Giovanni Decrescenzo, Mr. Rob Knudsen, Mr. Ryan Duff.

Finally, and most importantly is the appreciation I reserve for my family. I thank my sisters for their often words of encouragement that never did fall

on deaf ears. I am eternally grateful to my mother and father who have always given me the support and encouragement I have needed throughout my education. I can never repay that to them, but instead, I hope to make them proud.

Dedicated to Mom and Dad

TABLE OF CONTENTS

1	Introduction	16
1.1	Introduction and Theory	16
1.2	Motivation	16
2	Background	18
2.1	NMR	18
2.1.1	Intrinsic Spin and Spin Angular Momentum	18
2.1.2	Interaction with a Magnetic Field	20
2.1.3	Bulk Magnetization and Polarization	23
2.1.4	The \vec{B}_1 Excitation Field	29
2.1.5	The Phenomenological Bloch Equations	31
2.1.6	Rabi Oscillations	34
2.1.7	Free Induction Decay and Signal Detection	34
2.2	RF Coil Design	36
2.2.1	Receiver Coil Optimization	37
2.2.2	Tuning and Matching the Receiver Coil	37
2.2.3	Volume Coil	40
2.2.4	Birdcage Coil	42
3	Pulsed Rabi Measurements	43

3.1	Method for Pulsed Rabi Measurements	44
3.2	Results	45
3.3	Discussion	47
4	Direct Measurement of Rabi Oscillations	48
4.1	Modification of MR Scanner Software	49
4.2	Methodology and Circuitry for Inducing Rabi Oscillations . .	49
4.2.1	\vec{B}_1 -Transmit Birdcage Coil	50
4.2.2	Birdcage Coil Geometry, Tuning, and Matching	51
4.2.3	$\lambda/8$ Hybrid Coupler	53
4.2.4	\vec{B}_1 field mapping and field inhomogeneity calculation .	57
4.3	Methodology and Circuitry for Detecting Rabi Oscillations . .	61
4.3.1	Design Considerations	61
4.3.2	Circuit Simulations	62
4.3.3	Detection Coil Geometry, Tuning, and Matching	65
4.3.4	Circuit Construction	67
4.4	Experiments	68
4.4.1	Variation of \vec{B}_1 Amplitude	69
4.4.2	Dependency on Number of Nuclei	71
4.4.3	RF Coil Field Calibration	72
4.5	Results	79
4.5.1	Variation of \vec{B}_1 Amplitude	80
4.5.2	Dependency on Number of Nuclei	81

4.5.3	RF Coil Field Calibration	81
4.6	Discussion	84
4.6.1	Variation of \vec{B}_1 Amplitude	84
4.6.2	Dependancy on Number of Nuclei	85
4.6.3	RF Coil Field Calibration	86
4.6.4	Computer Calculation of Rabi Field Strength	89
5	Conclusion	91
	Appendices	96
A	The Rotating Frame of Reference	96
B	The Flip Angle	100
C	Spin Relaxation	101
D	RC Network	106
E	High-Pass Filter	107
F	Half-Wave Diode Rectifier	107
G	Birdcage Builder	108
H	Resonance Circuit Q Corrections to Induced Voltage	110

LIST OF FIGURES

1	Spin 1/2 state orientations.	21
2	Spin precession. A spin $\vec{\mu}$, precesses around \vec{B}_0 at the Larmor frequency. The direction of the precession is determined by the gyromagnetic ratio, γ	24
3	The Zeeman effect.	27
4	Circularly polarized field components of \vec{B}_1 . If the excitation frequency of the field \vec{B}_1 field is equal to the Larmor frequency, ω_0 , then \vec{B}_1^- can be neglected	31
5	Precession of bulk magnetization, \vec{M} in the Laboratory frame of reference	33
6	LC circuit diagram. Tuning capacitance (C_T) is added in parallel to the coil (L) while the matching capacitance (C_M) is added in series. R is the total resistance of the coil from all losses.	40
7	Birdcage coils in A) High Pass mode B) Low Pass mode C) Band Pass Mode [16]	41
8	Equivalent Circuits for birdcage coils in A) High Pass mode B) Low Pass mode C) Band Pass mode.	42
9	Plot of measured SNR vs \vec{B}_1 duration from ^1H peak from a 1L sample of water	45

10	Fourier transform of the data displayed in Figure 9 displaying a peak frequency component at 575Hz.	46
11	View of the ^1H -tuned \vec{B}_1 -Transmit Birdcage Coil	52
12	Signal phase shifting in a $\lambda/8$ hybrid coupler.	53
13	Equivalent circuit of a $\lambda/8$ hybrid coupler.	54
14	Completed lumped elements of the $\lambda/8$ hybrid coupler.	56
15	Normalized \vec{B}_1 map of a transverse slice at the centre of the coil.	58
16	(a) Normalized \vec{B}_1 field distribution in one slice of the map 4cm, and (b) histogram of the normalized \vec{B}_1 field throughout the centre region of the coil.	60
17	LTSpice Circuit Simulation. The final staged circuit configuration which lead to the simulated output of Figure 18: A. Thevenin equivalent of induced voltage source. B. RLC 'tank' circuit composed of detector coil (Figure 20). C. Half Wave Rectifier and RC integrator. D. High Pass filter to remove DC component of signal. E. Non-inverting amplifier with gain of 5.2.	63

18	LTSpice Circuit Simulation. A simulation was run where a 3V signal at a carrier frequency of 127.74MHz was modulated with a 0.3V signal oscillating at 575Hz and was simulated for 40ms (green trace). The blue line represents the voltage after the rectification and integration, and the red trace represents the output voltage after amplification.	64
19	Constructed circuit of Figure 17C, 17D, and 17E.	66
20	The Rabi detection coil. The Rabi detection circuitry outlined in Figure17B with a 30mL water sample placed inside.	67
21	MRI Experiment Set Up. The Birdcage coil used to produce the B_1 field is placed in the centre of the magnet and connected to the $\lambda/8$ hybrid coupler which is then fed to the DFG of the scanner. The detection coil is placed in the centre of the birdcage coil with its output being fed through an interface to outside the scanner room to the filter circuit (Figure 19) and then to an oscilloscope where data is recorded and visualized.	70
22	RF Coil Calibration Setup. Helmholtz pair (A.) set up oscillating at 575Hz, with an AC function generator (C.) which permits current through the coil to be varied. RF Detection coil (A) is placed in the centre of the Helmholtz pair and hooked up to the filtration circuit and oscilloscope (B) to measure induced voltage.	73

23	Scaled view of Figure 22A. The Rabi detection coil placed along the z-axis of the Helmholtz pair, simulating the experimental setup within the MRI. The Gauss meter (bottom) was then placed inside the coil to measure the magnetic field. . . .	74
24	Signal during the application of a \vec{B}_1 of $6.75\mu\text{T}$	75
25	Savitzky-Golay filtered signal during the application of a \vec{B}_1 of $6.75\mu\text{T}$. This data is the filtered result of Figure 24.	75
26	Fourier transformed signal during the application of a \vec{B}_1 of $6.75\mu\text{T}$. This is the Fourier transform of the data seen in Figure 25. A main Frequency component due to Rabi oscillations can be viewed at 288.2Hz.	76
27	Signal during the application of a \vec{B}_1 of $13.5\mu\text{T}$	76
28	Savitzky-Golay filtered signal during the application of a \vec{B}_1 of $13.5\mu\text{T}$. This data is the filtered result of Figure 27.	77
29	Fourier transformed signal during the application of a \vec{B}_1 of $13.5\mu\text{T}$. This is the Fourier transform of the data seen in Figure 28. A main Frequency component due to Rabi oscillations can be viewed at 573Hz.	77
30	Signal during the application of a \vec{B}_1 of $27\mu\text{T}$	78
31	Savitzky-Golay filtered signal during the application of a \vec{B}_1 of $27\mu\text{T}$. This data is the filtered result of Figure 30.	78

32	Fourier transformed signal during the application of a \vec{B}_1 of $27\mu\text{T}$. This is the Fourier transform of the data seen in Figure 31. A main Frequency component due to Rabi oscillations can be viewed at 1147Hz.	79
33	Rabi Oscillations with varied sample size. Signal spectra from an applied \vec{B}_1 field of $13.5\mu\text{T}$ with sample sizes of 0mL (top), 15mL (middle), and 30mL (bottom).	82
34	RF Detection Coil Calibration	83
35	Precession of the bulk magnetization, \vec{M} , in the laboratory frame of reference.	96
36	Precession of the bulk magnetization, \vec{M} , in the rotating frame of reference. When $\omega_{rf} = \omega_0$, the precession can be viewed simply as a tipping motion.	98
37	Precession of the bulk magnetization, \vec{M} , in the rotating frame of reference. When $\omega_{rf} \neq \omega_0$, precession occurs about \vec{B}_{eff} . . .	99
38	T_1 relaxation. At $t = T_1$, 63% of M_z has been recovered. . . .	102
39	T_2 relaxation. At $t = T_2$, M_{xy} has decayed to 37% of its maximum value.	105
40	Half-Wave Diode Rectifier. The use of the diode allows for only half the input waveform to be passed through.	108

41	(a) Coil specifications are defined to build a birdcage coil. (b) Calculated capacitance and position of the capacitors to be placed on the end ring. (c) Calculated self-inductance and effective inductance of the coil.	109
42	Circuit used in simulator for determining the quality Q of the frequency response.	110
43	Voltage response of the circuit in Figure 42 as a function of frequency.	111

LIST OF TABLES

1	RF Detection Coil Field Calibration (575Hz)	81
2	Rabi Field Calculation	89

1 Introduction

1.1 Introduction and Theory

This chapter provides the motivation for the work contained within this thesis. This chapter is intended to provide enough background information to understand the general goal of this thesis as well as the relevant background theory of MR and circuits used in this work.

1.2 Motivation

When a nuclear magnetic moment is placed an external static magnetic field, resonance is observed where the nuclear magnetic moment will precess about the axis of the applied field at the Larmor frequency. However when an additional oscillating magnetic field is introduced at the Larmor frequency, a secondary resonance is observed where the net magnetic moment will also precess about the axis of the applied field at the Rabi frequency. The Rabi frequency is a consequence of a quantum mechanical phenomena where the net nuclear magnetization will oscillate between parallel and anti-parallel alignment with the external magnetic field. A direct continuous measurement of this Rabi oscillation has not yet been conducted with a nuclear spin system, however indirect measurements have been conducted using a pulsed method [1, 2, 3]. Unfortunately, these studies provide no information with regards to strength of these oscillations. For field strengths typical of most clinical MR systems a nuclei's Larmor and Rabi frequencies are typically oscillating

in 100's of MHz and 100's of Hz respectively.

Carrier-mediated drug delivery has emerged as one of the most promising methods for biomedical applications of nanoparticles. The therapeutic index of drugs could be increased by enhancing the specificity due to the targeting to a particular tissue or cell, and the control over the release kinetics. Delivery of the drug can be activated through the destabilization of the carrier system by an external stimulus, which can be of different nature depending on the system. Recent investigations have also explored the capability of controlling the position or temperature of magnetic nanoparticles within cells and tissues by remote application of magnetic fields [4, 5, 6]. So far, this has only been investigated by manipulation of nanoparticles using alternating magnetic fields, or through rotating permanent magnets originating outside of the tissues of interest.

Recently in order to minimize the temperature contribution and investigate only the field effect, low-frequency alternating magnetic fields (LF-AMF), 0.1-5kHz, have been used for drug release from magnetic systems.[7, 8, 9, 10] Rotating magnetic fields at low frequencies such as 10-40Hz have been used to control rotation and movement of magnetic nanoparticles about their own axis causing the release and/or actuation of the attached therapeutic agent.

This work proposes that there exists a LF-AMF due to Rabi oscillations which can be directly measured in a clinical 3T MRI. The direct measurement and characterization of these Rabi oscillations is required to determine

if these oscillations can be used to manipulate magnetic nanoparticles. The detection, characterization and validation of this 'Rabi field' will be conducted through the course of this thesis.

2 Background

2.1 NMR

The basis of the NMR phenomenon relies on the magnetic properties of the protons and neutrons within the atomic nucleus. The most commonly used nucleus is that of Hydrogen (i.e. the proton ^1H) due to its abundance in the human body (98.98%) and its high NMR sensitivity. The principles of NMR can be described by a combination of quantum and classical models. From quantum mechanics atomic nuclei possess a property called spin, which is analogous to angular momentum from the classical model.

2.1.1 Intrinsic Spin and Spin Angular Momentum

There are many nuclei which exhibit intrinsic spin, which is a fundamental property of nature like charge and mass. Individual nucleons have spin $1/2$. The spins from the interacting nucleons couple together in the nucleus to form an entity with spin angular momentum $\hbar I$ where I is either an integer or half integer.

The proton and neutron have the same spin angular momentum as the electron, $\hbar/2$ but their magnetic moments (also referred to as spins) are much

smaller because of their far greater masses.

According to classical theory, and considering the dominant nuclei in MRI (the proton), the magnetic moment of the nucleus, $\vec{\mu}$, can be described as follows: A proton possesses a positive charge $+e$, which rotates about its axis due to its spin. This rotation generates an angular momentum which in turn gives rise to a magnetic moment $\vec{\mu}$. This process can be compared to a circulating charge through a coil of wire, which has the effect of producing a magnetic flux.

The magnetic moment associated with the total spin angular momentum $\hbar I$ can be written as:

$$\vec{\mu} = \frac{ge\hbar I}{2m_p} \quad (1)$$

where g is the Lande factor and is given by 5.586 for the neutron and -3.826 for the proton, e is the charge of an electron, m_p is the mass of the proton, and $\hbar = h/2\pi$. By defining the gyro-magnetic ratio γ as:

$$\gamma = \frac{ge}{2m_p} \quad (2)$$

The magnetic moment can be rewritten to:

$$\vec{\mu} = \gamma\hbar I \quad (3)$$

in which $\gamma = 2.675 \times 10^{10}$ rad s⁻¹ T⁻¹ for protons.

Since the magnetic moment is a vector quantity, its magnitude and ori-

entation need to be defined. The magnitude of $\vec{\mu}$ is denoted by μ :

$$\mu = \gamma\hbar\sqrt{I(I+1)} \quad (4)$$

Although the magnitude of $\vec{\mu}$ is certain under any condition (with or without an external magnetic field), its orientation is random in the absence of an external magnetic field due to random thermal motion.

2.1.2 Interaction with a Magnetic Field

In the presence of a magnetic field \vec{B}_0 , which by convention in MR is designated to be applied in the z-direction ($\vec{B}_0 = B_0\hat{z}$), the randomly orientated magnetic moments will tend to align with the magnetic field. As a consequence of the quantum model, the magnetic moment vectors do not line up exactly with the external magnetic field but instead assume a discrete set of orientations.

The z-component of $\vec{\mu}$ is now certain due to the \vec{B}_0 field and is defined for all possible orientations by:

$$\mu_z = \gamma m_I \hbar \quad (5)$$

where m_I is the magnetic quantum number having $2I + 1$ values representing the number of degenerate states for the atom:

$$m_I = -I, -I + 1, \dots, I \quad (6)$$

which in turn corresponds to $2I + 1$ possible orientations for $\vec{\mu}$ with respect to the direction of the external field. The angle θ between the magnetic moment and the applied magnetic field can be calculated using the following formula:

$$\cos\theta = \frac{\mu_z}{\mu} = \frac{m_I}{\sqrt{I(I+1)}} \quad (7)$$

For a spin $1/2$ system, $I = 1/2$, $m_I = \pm 1/2$ making $\theta = \pm 54^\circ 44'$. These two possible orientations are commonly referred to as parallel (spin up) and anti-parallel (spin down) states are shown in Figure 1.

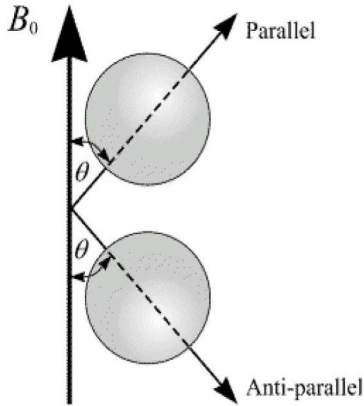


Figure 1: Spin $1/2$ state orientations.

A magnetic moment in an external magnetic field experiences a torque. The equation of motion for $\vec{\mu}$ is:

$$\frac{d\vec{\mu}}{dt} = \gamma\vec{\mu} \times \vec{B}_0 \quad (8)$$

The solution to (8) can be expressed by first re-writing the equation in scalar form as:

$$\begin{aligned} \frac{d\mu_x}{dt} &= \gamma B_0 \mu_y \\ \frac{d\mu_y}{dt} &= -\gamma B_0 \mu_x \\ \frac{d\mu_z}{dt} &= 0 \end{aligned} \quad (9)$$

By taking further derivatives with respect to time the first two equations decouple. The equations can now be given by:

$$\begin{aligned} \frac{d^2\mu_x}{dt^2} &= -\gamma^2 B_0 \mu_x \\ \frac{d^2\mu_y}{dt^2} &= -\gamma^2 B_0 \mu_y \end{aligned} \quad (10)$$

Setting the initial conditions to be $\mu_x(0), \mu_y(0)$, and $\mu_z(0)$, the solutions to these equations are:

$$\begin{aligned}
\mu_x(t) &= \mu_x(0)\cos(\gamma B_0 t) + \mu_y(0)\sin(\gamma B_0 t) \\
\mu_y(t) &= -\mu_x(0)\sin(\gamma B_0 t) + \mu_y(0)\cos(\gamma B_0 t) \\
\mu_z(t) &= \mu_z(0)
\end{aligned}
\tag{11}$$

which can be further expressed as:

$$\begin{aligned}
\mu_{xy}(t) &= \mu_{xy}(0)e^{-i\gamma B_0 t} \\
\mu_z(t) &= \mu_z(0)
\end{aligned}
\tag{12}$$

From these solutions it is evident that the transverse component of the magnetic moment precesses about \vec{B}_0 at a frequency:

$$\omega_0 = \gamma B_0
\tag{13}$$

known as the Larmor frequency (Figure 2).

2.1.3 Bulk Magnetization and Polarization

In 2.1.2 it was shown that an isolated magnetic moment placed in an external uniform magnetic field can assume one of a number of states determined by value m_I . Generally when involved with NMR imaging it is not just one magnetic moment (i.e. one proton) which is views but all the nuclei within

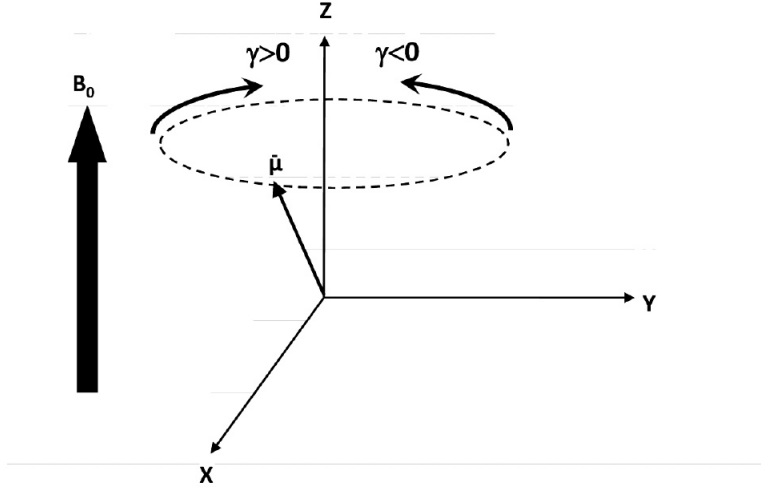


Figure 2: Spin precession. A spin $\vec{\mu}$, precesses around \vec{B}_0 at the Larmor frequency. The direction of the precession is determined by the gyromagnetic ratio, γ .

the region of interest. To describe the effect of a large number of magnetic moments a bulk (macroscopic) magnetization vector \vec{M} is introduced, which is the vector sum of all the individual (microscopic) magnetic moments over the volume, V . This summation is expressed by:

$$\vec{M} = \frac{1}{V} \sum_{n=1}^N \vec{\mu}_n \quad (14)$$

where N is the total number of magnetic moments in the object under scrutiny and $\vec{\mu}_n$ is the magnetic moment of an individual proton. The set of spins in V is called an isochromat which can be defined to be an ensemble

or domain of spins with the same phase.

The equation of motion for \vec{M} is given as:

$$\frac{d\vec{M}}{dt} = \gamma \vec{M} \times \vec{B}_0 \quad (15)$$

which can be resolved into three coupled linear differential equations which are valid for a homogeneous \vec{B}_0 field:

$$\begin{aligned} \frac{dM_x}{dt} &= \gamma(M_y B_z - M_z B_y) \\ \frac{dM_y}{dt} &= \gamma(M_z B_x - M_x B_z) \\ \frac{dM_z}{dt} &= \gamma(M_x B_y - M_y B_x) \end{aligned} \quad (16)$$

It shall now be considered how every magnetic moment in our ensemble behaves collectively when placed in a \vec{B}_0 field.

Magnetic moments occupying the two possible states will have a potential energy given by:

$$E = -\vec{\mu} \cdot \vec{B}_0 \quad (17)$$

Keeping with the convention that the applied magnetic field is taken to lie along the z-direction (17) can be rewritten

$$E = -\gamma \hbar m_I B_0 \quad (18)$$

The energy associated with the spin up state ($m_I = +1/2$) is given by:

$$E_+ = -\frac{1}{2}\gamma\hbar B_0 \quad (19)$$

whereas for spin down state ($m_I = -1/2$) the potential energy is:

$$E_- = \frac{1}{2}\gamma\hbar B_0 \quad (20)$$

Equations (19) and (20) indicate that the lower energy level is associated with the spin up state resulting from magnetic moments aligning themselves parallel to the applied magnetic field as opposed to anti-parallel for the spin down state. The difference between the energy states is given by:

$$\Delta E = E_- - E_+ = \gamma\hbar B_0 \quad (21)$$

a phenomenon known as the Zeeman effect, shown in Figure 3.

For a transition between the two energy states, quanta of energy equal to $\gamma\hbar B_0$ must be absorbed or emitted. This corresponds to electromagnetic radiation of angular frequency ω_0 with energy $\hbar\omega_0$. Equating the energy of the electromagnetic radiation with the difference between the energy states the result is the previously defined Larmor equation given by (13).

In thermal equilibrium, the population distribution between the two energy states is given by the Maxwell-Boltzman distribution. The populations of both states are given by:

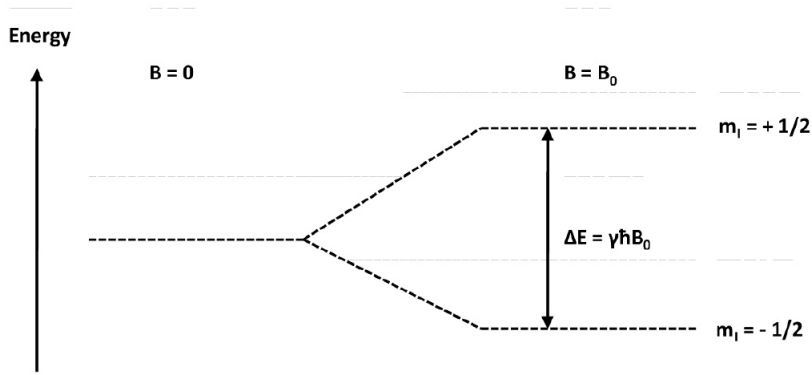


Figure 3: The Zeeman effect.

$$\begin{aligned}
 N_+ &= \frac{N}{2} e^{\frac{\gamma\hbar B_0}{2k_B T}} \\
 N_- &= \frac{N}{2} e^{-\frac{\gamma\hbar B_0}{2k_B T}}
 \end{aligned}
 \tag{22}$$

where N is the total number of spins, k_B is the Boltzmann constant, T is the temperature in Kelvin, N_+ and N_- represent the number of spins in the spin-up (parallel) and spin-down (anti-parallel) orientation with respect to the external field. By defining the difference in the population of the two energy states under the high temperature approximation:

$$N_+ - N_- = \frac{N\gamma\hbar B_0}{2k_B T}
 \tag{23}$$

it can be seen that there is an excess fraction of spins in the lower energy

level spin up state. Thus only a small portion of the total population of magnetic moments contribute to the bulk magnetization vector. The bulk magnetization vector can therefore be expressed as:

$$\vec{M} = N\vec{\mu}P \quad (24)$$

where P is the polarization of the ensemble of spins and is defined as:

$$P = \frac{N_+ - N_-}{N_+ + N_-} \quad (25)$$

The polarization due to a Maxwell-Boltzman distribution of spins under the high temperature approximation is given by:

$$P = \tanh\left(\frac{\gamma\hbar B_0}{2k_B T}\right) \approx \frac{\gamma\hbar B_0}{2k_B T} \quad (26)$$

Therefore the magnitude of the magnetization vector is found to be:

$$M = M_0 = \frac{N\gamma^2\hbar^2 B_0}{4k_B T} \quad (27)$$

and for a spin- I system M is:

$$M = M_0 = \frac{N\gamma^2\hbar^2 B_0 I(I+1)}{3k_B T} \quad (28)$$

It can be seen from (27) and (28) that M_0 is the equilibrium magnetization and the spin system establishes with its environment. It is evident from (26) that the polarization increases linearly with frequency and therefore with

magnetic field strength. For protons in a 1.5T field at 300K, the polarization is only $5.1 \times 10^{-4}\%$.

2.1.4 The \vec{B}_1 Excitation Field

As described previously, in Magnetic Resonance (MR), the bulk magnetization vector, \vec{M} , results from emersion in the main static field, B_0 . The signal acquired during an MR experiment requires the magnetization vector to contain a components in the plane perpendicular to the axis of the static field B_0 . Details of this acquisition will be described in section 2.1.7. In order to perturb \vec{M} from its equilibrium position, a second magnetic field is applied in the transverse plane (\hat{x}, \hat{y}) perpendicular to the main static field.

This so called excitation field comes in the form of a time dependant (i.e. oscillating) magnetic field denoted as \vec{B}_1 . As previously stated in 2.1.3, supplying energy to an ensemble of spins in quanta of $\hbar\omega_0$ causes transitions to occur resulting in emission or absorption of energy. It therefore becomes evident that in order to induce a transition between energy states, the \vec{B}_1 field oscillation frequency, ω_{rf} , must be equal to the Larmor frequency of the system which is determined by the static field. This is known as the resonance condition. Introduction of the \vec{B}_1 field introduces phase coherence to the spin system and allows for the net magnetic moment of the system to be used.

A typical \vec{B}_1 excitation field is linearly polarized and expressed in the form of:

$$\vec{B}_1 = 2B_1^e \cos(\omega_{rf}t + \phi) \hat{x} \quad (29)$$

for pulse envelope B_1^e , excitation carrier frequency ω_{rf} , and initial phase angle ϕ . This linearly polarized field can be decomposed into two circularly polarized field rotating in opposite directions, shown as:

$$\vec{B}_1 = \vec{B}_1^+ + \vec{B}_1^- \quad (30)$$

\vec{B}_1^+ and \vec{B}_1^- are given by:

$$\begin{aligned} \vec{B}_1^+ &= B_1^e [\cos(\omega_{rf}t + \phi) \hat{x} - \sin(\omega_{rf}t + \phi) \hat{y}] \\ \vec{B}_1^- &= B_1^e [\cos(\omega_{rf}t + \phi) \hat{x} + \sin(\omega_{rf}t + \phi) \hat{y}] \end{aligned} \quad (31)$$

where \vec{B}_1^+ rotates clockwise and \vec{B}_1^- rotates anti-clockwise (Figure 4).

It can be shown that the only component of the \vec{B}_1 field that is rotating in the same direction as the bulk magnetization, represented by \vec{B}_1^+ field in (31) has a considerable effect. This is because the circularly polarized field rotating in the opposite direction, represented by the term \vec{B}_1^- , is always off resonance and if ω_{rf} is near the Larmor frequency then this term can be neglected since it has minimal effect on precessing bulk magnetization. The \vec{B}_1^+ field is referred to as the transmit field.

The \vec{B}_1 field strength required for a linear polarized field is twice that

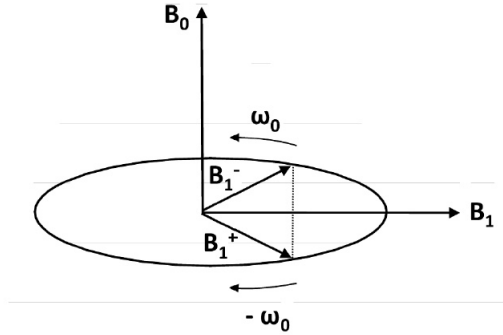


Figure 4: Circularly polarized field components of \vec{B}_1 . If the excitation frequency of the field \vec{B}_1 is equal to the Larmor frequency, ω_0 , then \vec{B}_1^- can be neglected

of a circularly polarized field which is why many modern MRI systems use quadrature transmitter coils to generate a circularly polarized field directly, thereby reducing the power deposition within the sample.

2.1.5 The Phenomenological Bloch Equations

By combining the equation of motion in section 2.1.4 with the relaxation equations in Appendix C the complete equations of motion for the magnetization vector in the laboratory frame are obtained:

$$\begin{aligned}
\frac{dM_x}{dt} &= \gamma(M_y B_z - M_z B_y) - \frac{M_x}{T_2} \\
\frac{dM_y}{dt} &= \gamma(M_z B_x - M_x B_z) - \frac{M_y}{T_2} \\
\frac{dM_z}{dt} &= \gamma(M_x B_y - M_y B_x) - \frac{M_z - M_0}{T_2}
\end{aligned} \tag{32}$$

These are the Bloch equations [11] which in vectorial notation can be written as:

$$\frac{d\vec{M}}{dt} = \gamma \vec{M} \times \vec{B}_0 - \frac{M_x \hat{x} + M_y \hat{y}}{T_2} - \frac{M_z - M_0}{T_1} \hat{z} \tag{33}$$

and in the rotating reference frame (Appendix A) written as:

$$\frac{\partial \vec{M}}{\partial t} = \gamma \vec{M} \times \vec{B}_{eff} - \frac{M_{x'} \hat{x}' + M_{y'} \hat{y}'}{T_2} - \frac{M_z - M_0}{T_1} \hat{z} \tag{34}$$

In the presence of an RF pulse, $\vec{B}_1 = B_1 \hat{x}$, the Bloch equations in the rotating frame of reference can be written out explicitly:

$$\begin{aligned}
\frac{dM_{x'}}{dt} &= \gamma M_{y'} \left(B_0 - \frac{\omega_{rf}}{\gamma} \right) - \frac{M_{x'}}{T_2} \\
\frac{dM_{y'}}{dt} &= \gamma M_{z'} B_1 - \gamma M_{x'} \left(B_0 - \frac{\omega_{rf}}{\gamma} \right) - \frac{M_{y'}}{T_2} \\
\frac{dM_{z'}}{dt} &= \gamma M_{y'} B_1 - \frac{M_{z'} - M_0}{T_2}
\end{aligned} \tag{35}$$

When the resonance condition is satisfied ($\omega = \omega_0$), and the initial condition of , $M(0) = M_0\hat{z}$, (35) has solutions:

$$\begin{aligned}
 M_x(t) &= M_0 \sin(\omega_1 t) \sin(\omega_0 t) \\
 M_y(t) &= M_0 \sin(\omega_1 t) \cos(\omega_0 t) \\
 M_z(t) &= M_0 \cos(\omega_1 t)
 \end{aligned}
 \tag{36}$$

where ω_1 is the Rabi frequency. These equations trace out the path along the surface of a sphere spiralling between $+\hat{z}$ and $-\hat{z}$ at ω_1 , while simultaneously oscillating about the \hat{z} -axis at ω_0

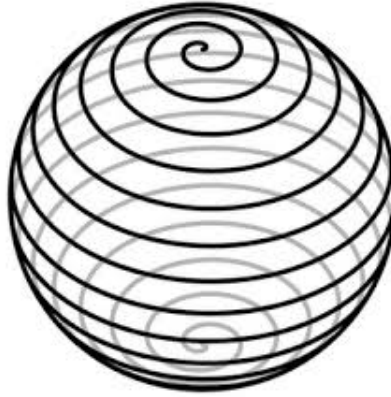


Figure 5: Precession of bulk magnetization, \vec{M} in the Laboratory frame of reference

2.1.6 Rabi Oscillations

The Rabi oscillation is the cyclic behaviour of a two-state quantum system in the presence of an oscillatory driving field. In the context of NMR, a magnetic spin in a static magnetic field modulated by a radio frequency field will cause the spin vector to oscillate between anti-parallel and parallel with respect to the static field. [12]. These oscillations are referred to as Rabi oscillations, or Rabi flopping. Similar to (13), the frequency of Rabi oscillations is defined by:

$$\omega_1 = \gamma \vec{B}_1 \quad (37)$$

In contrast to conventional NMR acquisition, observation of signal due to Rabi oscillation is only observable during the application of the \vec{B}_1 field. The applied \vec{B}_1 is much weaker than the static \vec{B}_0 which leads to a frequency separation of $\sim 10^6$ Hz between ω_1 and ω_0 .

In the laboratory frame of reference (36) demonstrates that Rabi oscillations occur as an amplitude modulation of the transverse magnetization along with direct oscillation of the z-component of magnetization. This realization is important to the measurement of such oscillations.

2.1.7 Free Induction Decay and Signal Detection

Once tilted away from the z' -axis, the transverse component of \vec{M} becomes a rotating vector (i.e. it precesses) which generates an oscillating RF field

that can be detected using a suitable receiver coil. These coils are tuned and matched with capacitors such that the electronic resonance matches the Larmor frequency. The coils used for the work in this thesis are presented in Section 4.

The amplitude of the oscillating RF field decays exponentially with an envelope of $e^{-\frac{t}{T_2}}$. The initial amplitude of this field is determined by how much transverse magnetization is generated and therefore dependant on the flip angle. The precession of the transverse magnetization observed as an induced electromotive force across the receiver coil, this is known as the Free Induction Decay (FID).

The induced voltage in the coil, ignoring relaxation effects is given by:

$$V(t) = -\omega_0 \int |M_{xy}(\vec{r})| |B_1^-(\vec{r})| \sin[\omega_0 t + \Phi_0(\vec{r}) - \Phi_{B_1}(\vec{r})] d\vec{r} \quad (38)$$

(39) explicitly shows that the detection signal voltage is dependant on the transverse magnetization in the laboratory frame, $M_{xy}(\vec{r})$, at $t = 0$, the sensitivity of the receiver coil $B_1^-(\vec{r})$, in the transverse plane, and the precession frequency, ω_0 , the Larmor frequency in this example, however in the case of measuring Rabi oscillations would be replaced by ω_1 . The terms $\Phi_0(\vec{r})$ and $\Phi_{B_1}(\vec{r})$ represent the phase of the transverse magnetization at $t = 0$ and the phase of the receiver coil respectively.

Interpolation of a time domain response such as a FID becomes difficult when a number of frequencies are contained within it. It is often easier to

interpret the complex signal, $S(t)$, once it has been Fourier transformed into the frequency domain, $S(\omega)$ by:

$$S(\omega) = \int_0^{\infty} e^{i\omega t} dt \quad (39)$$

The Fourier transform allow each individual frequency contained within the signal to be assigned specific sinusoidal and cosinusoidal components in the frequency domain.

2.2 RF Coil Design

The receiver coils used during direct Rabi measurements have all been built in house. There are a wide variety of coil designs employed in MRI, with the design of the coil being dependent on what is being measured. The majority of coils can be categorised as either surface or volume coils which can be used to transmit, receive, or transmit and receive radiofrequency (RF) signals.

To generate a \vec{B}_1 field the transmit coil produces a pulse defined by Ampere's Law [13]:

$$\frac{1}{\mu_0} \oint B_1 \cdot dl = \int_S J \cdot dS \quad (40)$$

where J is the current density through the coil, and S is the surface of the coil which the B_1 field is transmitted from.

Signal reception occurs when precessing magnetization induces an elec-

tromotive force (EMF), ξ , in the coil through Faraday induction:

$$\xi = -\frac{d}{dt} \int_S B \cdot dS = -\int_V \left(\frac{dM(r)}{dt} \right) B_c(r) \cdot dV \quad (41)$$

where B refers to the magnetic field produced by the precessing magnetization, M , at a given position, r . B_c is the coil sensitivity, defined as the magnetic field that would be produced by the receive coil per unit current, and V is the volume of the sample. Coil sensitivity is determined by design, ideally it should be homogeneous across the sample.

2.2.1 Receiver Coil Optimization

In order to maximize the received signal two important properties of the coil require optimization. The first is that all loss mechanisms should be minimized to achieve a high sensitivity. The second, which has previously been mentioned, is that the geometry of the coil should correspond to the geometry of the sample. This is quantified by the filling factor. [14]

2.2.2 Tuning and Matching the Receiver Coil

The receiver coil should be tuned to the resonant frequency of the appropriate nucleus. If the coil is not correctly tuned there will be a suboptimal transfer of energy from the resonant nuclei in the imaged volume to the receiver which will result in the detected MR signal being reduced. The impedance of the coil must also be matched to the 50Ω input impedance

of the pre-amplifier to minimize reflection of signal. The fraction of signal reflected at the interface between the two circuits can be described by the reflection coefficient, Γ , as given by the equation:

$$\Gamma = \frac{Z_1 - Z_2}{Z_1 + Z_2} \quad (42)$$

Z_1 and Z_2 are the impedances of the coil circuit and the pre-amplifier. When Z_1 and Z_2 are equal, Γ goes to zero and thus the maximum transfer of signal is achieved.

In order to tune and match the designed receiver coils, a Network Analyser was used. This piece of apparatus can transmit a signal over a range of frequencies to the coil and then plot the reflection coefficient as a function of frequency. All the receiver coils in use were tuned to the resonant frequency of water at 3 T (i.e. the field strength of our magnet).

The resonant frequency is determined from the Larmor equation and therefore the resonant frequency of the RLC circuit must be tuned to this frequency. The resonant frequency of a parallel tuned RLC circuit is defined as:

$$\omega = \sqrt{\frac{1}{LC} - \frac{R^2}{L^2}} \quad (43)$$

where L and C are the inductance and capacitance and R is the equivalent parallel resistance of the circuit (including the coil resistance). Tuning is achieved by soldering high voltage capacitors in parallel with the coil. The

first step is to determine the inductance of the coil by observing the resonant frequency of the circuit on the Network Analyser for a capacitance of known value. With the inductance now known, (43) was used to calculate a value of capacitance (C_T) that would tune the coil to the Larmor frequency.

The impedance of the coil is matched to 50Ω by adding larger capacitors in series with the coil. The Network Analyser is used to display a Smith chart to make matching easier. When the impedance contour of the circuit overlays the 50Ω contour shown on the display the coil is matched. The better matched the LC circuit, the larger the dip of the resonant frequency as observed in the trace of the Network Analyser.

With the coil matched to 50Ω , C_T needed to be re-adjusted since the addition of the matching capacitance C_M had changed the resonant frequency of the coil. The required total capacitances for C_T and C_M were thereby found through an iterative process since altering C_T would also alter the impedance and so C_M would need to be adjusted once again. An LC circuit diagram to which all the receiver coils built in this thesis conform to is illustrated in Figure 6.

Once the coil had been tuned to the specific MR nucleus and matched to 50Ω , crossed diodes were connected in parallel with the coil to protect the preamplifier from large voltages during transmission. Before reaching the receiver input of the MR console, the small voltages picked up by the coil were passed through the preamplifier.

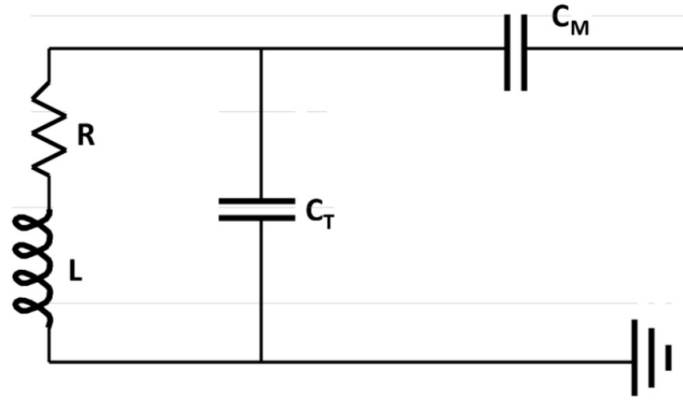


Figure 6: LC circuit diagram. Tuning capacitance (C_T) is added in parallel to the coil (L) while the matching capacitance (C_M) is added in series. R is the total resistance of the coil from all losses.

2.2.3 Volume Coil

While transmitting RF pulses, the coil is expected to be able to generate a uniform magnetic field over a specified volume.

Earlier volume coils were built using a linear modality. In this configuration, both transmission and reception took place along a single axis. When the RF pulse is fed through a single port in linear mode, a linear polarized \vec{B}_1 field is generated. The linear oscillating field can be decomposed into two counter-rotating circular fields, one in the same direction and frequency as the NMR spin system, and the other in the opposite direction. The opposite rotating field does not contribute at all with the spins, leading to wastage of power. In the transmit mode linear polarized coils are inefficient such that

half their power is wasted, and thus while receiving, they are incapable of extracting full phase information from the MR signal.

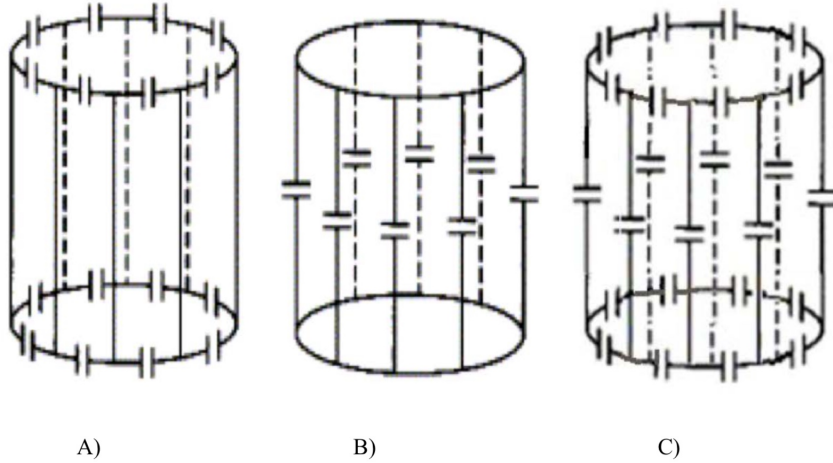


Figure 7: Birdcage coils in A) High Pass mode B) Low Pass mode C) Band Pass Mode [16]

Alternatively, in the quadrature mode, a coil can be fed with two signals that have a 90° phase shift, creating a circular polarized magnetic field. During the excitation, the field rotates in the same direction with the spin precessions. The quadrature coil will have half the power requirement for the excitation compared to the linearly polarized field generated by linear mode.

Volume coils are advantageous to surface coils when \vec{B}_1 homogeneity is of concern, however produce lower SNR when compared to surface coils. A uniform rotational magnetic field can be ideally generated by a uniform current distribution on a cylindrical surface.

2.2.4 Birdcage Coil

Hayes et al. [15] were the first to design birdcage coils. These are extensively used in the field of MRI because they provide a circular polarized field with high homogeneity. These coils are constructed with multiple parallel conductive segments (rungs) that are parallel to the magnetic field B_0 . The rungs are connected with a pair of end rings. Capacitors can be placed either on the rungs (Low pass) or on the end rings (High pass) or on both (Band pass) as shown in Figure 7a and 7b. L_1 represents the equivalent inductance on the end ring segment, C is the tuning capacitor, and L_2 is the equivalent inductance on the legs.

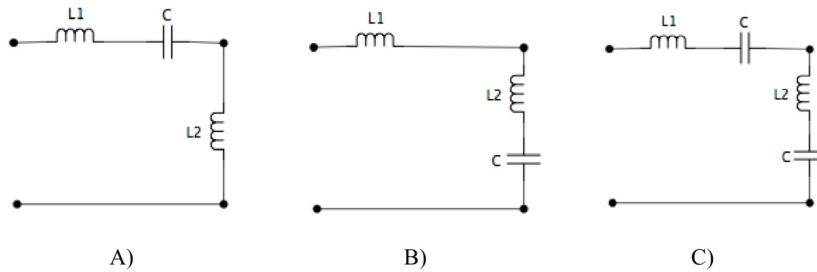


Figure 8: Equivalent Circuits for birdcage coils in A) High Pass mode B) Low Pass mode C) Band Pass mode.

3 Pulsed Rabi Measurements

To initially demonstrate and verify the Rabi oscillation of nuclear magnetization due to an applied \vec{B}_1 field, a pulsed measurement technique first suggested by Layton et. al. is attempted [1]. A \vec{B}_1 pulse of constant amplitude is used to excite a a sample of nuclei which will begin to oscillate. After some time, τ , the pulse will be shut off and the FID will be acquired. This process will be repeated, however each time the pulse duration (i.e. Flip angle, Appendix B) will be incrementally increased.

To process the data into a more useful form, each FID will be Fourier transformed into the frequency domain, where the SNR of the main peak will be calculated as defined by:

$$SNR = \frac{\mu}{\sigma} \quad (44)$$

where μ is the average of the points above half the maximum value of the signal under analysis, and σ is the standard deviation of a region of noise. Each SNR will be paired with the corresponding τ , creating a set of signal values as a function of applied \vec{B}_1 time. Finally, Fourier transforming this dataset displays it's oscillation frequency i.e. the Rabi frequency.

This method, although effective, acts only as a pseudo-measurement of observed Rabi oscillation as the signal being observed is due to the decay of the transverse component of the magnetization. Despite this, useful information can still be identified such as oscillation frequency, and decay.

3.1 Method for Pulsed Rabi Measurements

Throughout this work MR experiments have been conducted with the use of a Philips Acheiva 3T Magnetic Resonance Scanner at Thunder Bay Regional Health Sciences Centre (Figure 21). When transmitting a \vec{B}_1 field with this scanner's quadrature body coil (QBC) housed within the scanner itself, a maximum field strength of $B_1 = 13.5\mu T$ is possible, corresponding to a Rabi oscillation in the water protons ($\gamma = 42.577\text{MHz/T}$) at $\omega_1 = 574.79\text{Hz}$.

A 1L sample of water was placed in the centre of the magnet bore and produced a signal with a high signal to noise ratio (SNR). Keeping the \vec{B}_1 constant at $13.5\mu T$, a flip angle series was performed starting with $\alpha = 30^\circ$, a TR = 10 seconds ($\sim 5 \times T_1$), and $\Delta\alpha = 30^\circ$ for 120 iterations. Applying a constant \vec{B}_1 amplitude and incrementally increasing the flip angle, the duration of \vec{B}_1 can be directly controlled. Considering an initial flip angle of $\alpha = 30^\circ$ and increasing the flip angle by $\alpha = 30^\circ$ each iteration allows for the sample time to be ranged from 0.145ms to 17.4ms.

To create a single point in Figure 9, the protocol as outlined in Section 3 is followed, and a dataset of SNR values as a function of \vec{B}_1 field duration is acquired (Figure 9). SNR values from every-other period were assigned negative values as (45) only yields only an absolute value, so by assigning negative values to every-other cycle allows for the true oscillation to be observed. This dataset is then Fourier transformed (Figure 10) where the oscillation frequency can be visualized.

3.2 Results

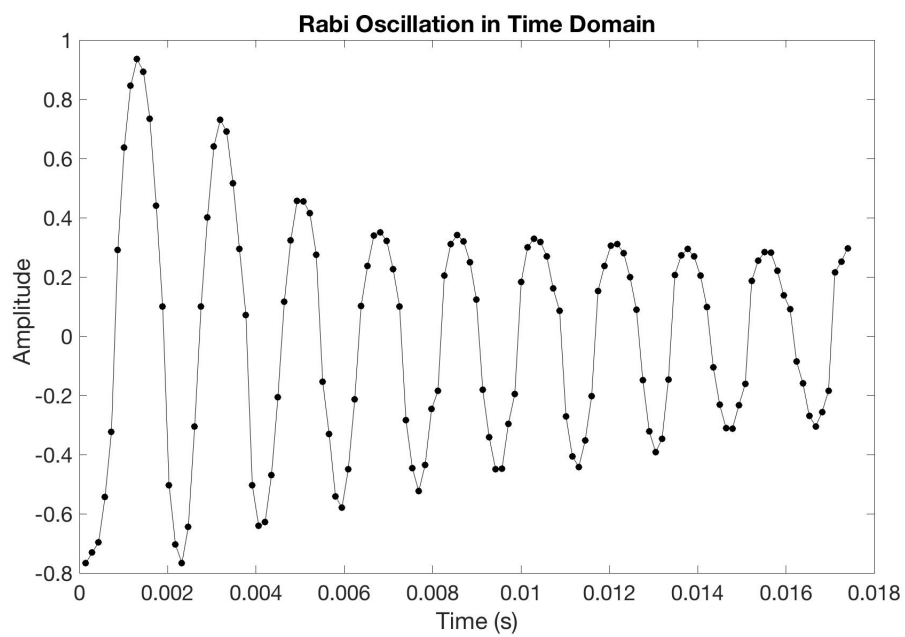


Figure 9: Plot of measured SNR vs \vec{B}_1 duration from ^1H peak from a 1L sample of water

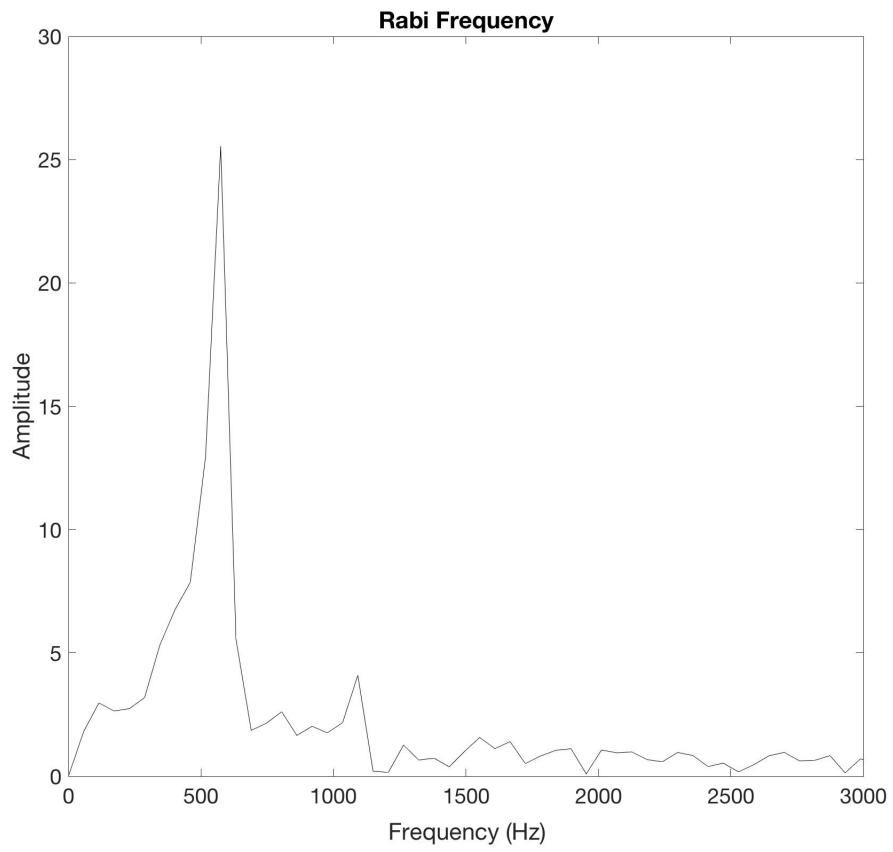


Figure 10: Fourier transform of the data displayed in Figure 9 displaying a peak frequency component at 575Hz.

3.3 Discussion

As the length of the applied \vec{B}_1 was increased the amount of signal due to magnetization in the transverse plane oscillated back and forth at the Rabi frequency (Figure 9). The Fourier transform of this dataset permitted the frequency components to be viewed (Figure 10), where a main peak at 575Hz is observed. Subsequent harmonic peaks are seen at integer-multiples of the Rabi frequency, which agrees with previously reported results [1, 2, 3].

Although this result gives confirmation that the Rabi oscillation occurs within the spin system, it gives no insight as to the strength of the oscillating field. This will be the goal of the remaining work.

It is important to note that this measurement acts as only a 'pseudo' measurement of Rabi oscillation, since the measured 'oscillation' as viewed in Figure 9 is composed of separate SNR values from multiple different measurements. In order to obtain information regarding strength of these oscillations a direct measurement must be conducted in order to truly characterize the 'Rabi Field'.

4 Direct Measurement of Rabi Oscillations

Direct measurement of Rabi oscillation is complicated by its time coincidence with the applied \vec{B}_1 field. Traditional MR measurement of nuclear precession is acquired after the conclusion of the \vec{B}_1 field. Often there is a delay to allow for a complete decay of the \vec{B}_1 power before signal acquisition is performed. Early attempts using the coils designed in this work determined that the high voltage signal due to direct \vec{B}_1 , high-frequency components ($\sim 40 V_{pp}$) would overpower the smaller induced voltages due to Rabi oscillations ($\sim 50 mV_{pp}$). Thus signal conditioning as discussed in Section 3.4 are pursued.

Due to software and hardware limitations of clinical MR systems, many are unable to carry out signal acquisition during the application of the radio-frequency (RF) field. Consequently stand-alone detection circuitry is required for direct measurement of Rabi oscillation. Induced voltages attributed to direct RF exposure far outweigh that due to Rabi precession by three orders of magnitude. As a result of this, detection circuitry will need to greatly attenuate high-frequency signal components while simultaneously amplifying frequencies in the low-frequency regime. Additionally, typical clinically used RF pulses use flip angles of 90 degrees ($\pi/2$ -pulse) or 180 degrees (π -pulse). These pulses tend to be very short in duration making them ineffective for the study of Rabi oscillations, where long pulse durations (high flip angle) are of interest.

This chapter discusses at length the alterations made to a clinical MR

scanner to enable the measurement of Rabi oscillations, outlining various coils made and the filter system used.

4.1 Modification of MR Scanner Software

Typical magnetic resonance imaging and spectroscopy utilize short RF pulses on the order of a few milliseconds to apply a B_1 field to a spin system. The Philips Acheiva 3T Magnetic Imaging system being used for these experiments has a manufacturer limit set on the pulse duration of 3.4ms ($\alpha = 720^\circ$) when the maximum B_1 field of $13.5\mu\text{T}$ is applied. To adequately characterize Rabi oscillations many cycles are required ($\alpha > 3600^\circ$) in order to maximize detected signal. In order to tailor this clinical system the unique needs of a Rabi measurement, alterations to the scanner's software were needed in the form of a "patch". This patch acts as a modular reference for the scanner upon startup which takes the scanner away from the default clinical mode, and allows for the maximum pulse duration to be increased up to 150ms ($\alpha = 30,000^\circ$) without risk of damaging the hardware.

4.2 Methodology and Circuitry for Inducing Rabi Oscillations

In order to detect a low frequency Rabi modulation of a low-voltage signal, in the presence of a very high-voltage B_1 transmit signal, a combination of circuit elements was used to achieve this goal. This section discusses each

element and various simulations which enabled the results of this work.

Section 2.1.5 demonstrated the signal contribution from the low-frequency Rabi oscillation occurs as a modulation to the high-frequency signal during the application of an \vec{B}_1 field. The signal components of the induced voltage ($V_{induced}$) can be broken up into the following components:

$$V_{induced} = V_{\omega_0,direct} + V_{\omega_0,sample} + V_{\omega_1,sample} \quad (45)$$

where, $V_{\omega_0,direct}$ is the induced voltage due to the direct exposure to the B_1 transmit field oscillating at ω_0 , $V_{\omega_0,sample}$ is the induced voltage due to the net nuclear magnetic moments within the sample also oscillating at ω_0 , and $V_{\omega_1,sample}$ is the induced voltage in the coil due to the net nuclear magnetization precessing at the Rabi frequency. With:

$$V_{\omega_0,direct} \gg V_{\omega_0,sample} + V_{\omega_1,sample} \quad (46)$$

substantial attenuation and filtration of high frequency ω_0 is required in demodulation of Rabi oscillation.

4.2.1 \vec{B}_1 -Transmit Birdcage Coil

Section 3.1 saw the use of the QBC of the MR scanner used as the source of the transmitted \vec{B}_1 . The transmission of RF through the QBC is subject to several manufacturer-imposed limits on both \vec{B}_1 field strength and duration. To circumvent these limits, a quadrature driven ^1H birdcage coil was designed

and built for this work. This work was essential to the varied \vec{B}_1 field strength experiments found in Section 4.4.1 where fields in excess of those clinically allowed are used.

4.2.2 Birdcage Coil Geometry, Tuning, and Matching

An 8-rung birdcage coil was built using copper tape sticking to the surface of a machined acrylic tube (Figure 11). The dimensions of the coil were carefully designed for an optimized filling factor. The diameter of the tube is 90mm with a length of 220mm. The end-ring width and the width of the rungs are both 6.5mm and the length of the rungs is 175mm. The extra space on the surface of the acrylic was reserved for tuning and matching circuit deployment. Eight gaps were made on each end-ring to accommodate all 16 capacitors, forming a high-pass structure as discussed in Section 2.2.4.

In order to tune the Birdcage to 127.74MHz (The Larmor frequency of ^1H at 3T), calculations for the end-ring tuning capacitor values were performed using the BirdcageBuilder software [16, 17]. With the dimensions specified above, the value of each end-ring capacitor is calculated to be 75pF. After 16 tuning capacitors were placed on the end rungs, the resonant frequency of the birdcage coil was measured using two RF-pick up probes previously tuned to 127.74MHz on a HP 8751A network analyzer. Specifically, the two pick-up probes were connected to the two ports of the network analyzer, and the two probe heads were placed across the birdcage coil. The network analyzer was set at a centre frequency of 127.74MHz with 10MHz span, in order to include

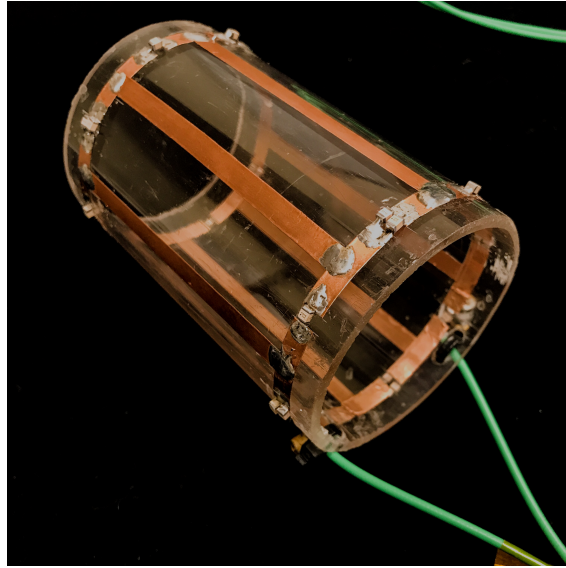


Figure 11: View of the ^1H -tuned \vec{B}_1 -Transmit Birdcage Coil

only the dominant resonance mode of the coil.

As discussed in section 2.2.2, to minimize the power reflection, the impedance of a coil at its input / output port should be matched to that of the device it is electrically connected to, such as the network analyzer, the scanner, a transmission line, or a hybrid coupler. There're many different ways to transform the input impedance of a coil to a desired value. In this work, a variable matching capacitor was placed at each quadrature port of the coil. Each port was connected to the network analyzer where the matching capacitor was adjusted until a resistance value of 50Ω was read on the smith chart at 127.74MHz.

4.2.3 $\lambda/8$ Hybrid Coupler

Hybrid coupler is a particular kind of directional coupler that divides the input power equally for two outputs. There are many ways to implement a hybrid coupler for microwave frequencies [18]. As described before, in order to implement a quadrature driving method, one needs to create two transmit signals of the same amplitude having a 90-degree phase shift. A $\lambda/8$ hybrid coupler was used in its lumped elements equivalent circuit for such an implementation as it maintains a compact device dimension. Figure 12 shows the structure of a $\lambda/8$ hybrid coupler built with two transmission lines of the standard characteristic impedance, where $C = 1/Z_0\omega$

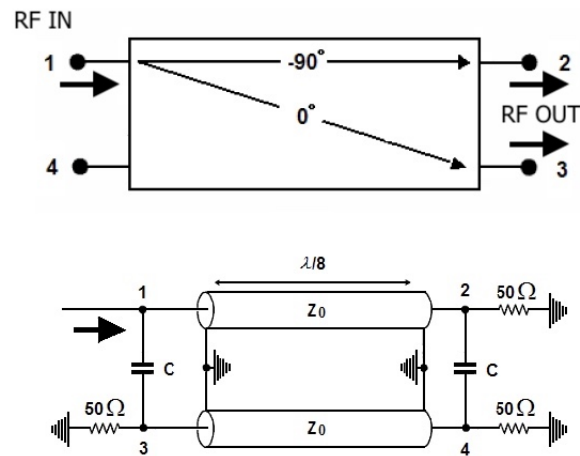


Figure 12: Signal phase shifting in a $\lambda/8$ hybrid coupler.

As previously mentioned, the Larmor frequency of ^1H in a 3T magnetic field at 127.74MHz which corresponds to a $\lambda/8$ of 29.34cm. To make the

hybrid circuit a minimum size, the two original transmission lines were replaced using lumped equivalent circuit elements. As shown in Figure 13, the $\lambda/8$ transmission lines are replaced by the π -network equivalent circuit, illustrated in the dashed line box. Obviously C_1 equals to C in Figure 12, and is $1/Z_0\omega$. To calculate the values of C_2 and L , which are components of the π -network, the equations below are used, given that all the ports are matched to 50Ω .

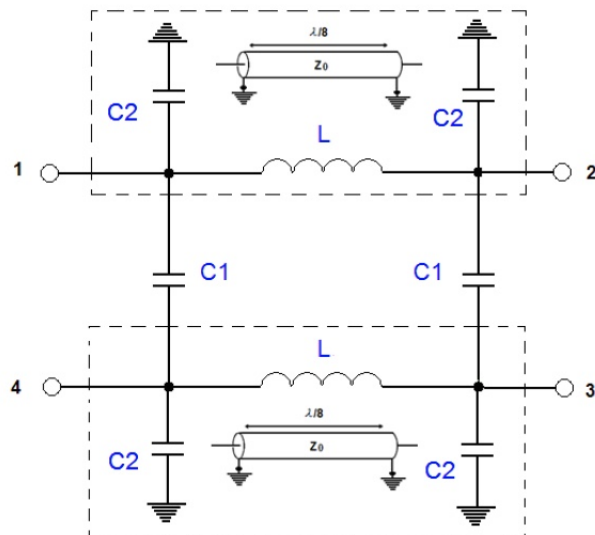


Figure 13: Equivalent circuit of a $\lambda/8$ hybrid coupler.

$$X_C = \frac{Z_0}{K} \quad (47)$$

$$X_L = Z_0 \frac{2K}{K^2 + 1} \quad (48)$$

The value of K can be determined by a condition derived from the character of the transmission line, that is, a $\lambda/8$ transmission line of characteristic impedance of Z_0 will exhibit an impedance of jZ_0 when shorted. Hence,

$$\frac{1}{jZ_0} = \frac{1}{j\omega L} + j\omega C_2 \quad (49)$$

From (47) & (48), the values of L and C_2 are obtained:

$$L = \frac{Z_0 \sqrt{2}}{2\omega} \quad (50)$$

$$C_2 = \frac{\sqrt{2} - 1}{Z_0 \omega} \quad (51)$$

By substituting the frequency ω into equations (50) & (51), the values of C_1 , C_2 , and L can be easily calculated. In this work, C_1 was calculated to be 25pf, C_2 was calculated to be 10pf, and L was calculated to be 44nH. The hybrid coupler was built on a PCB from Clinical MR Solutions (Figure 14). Inductors were winded on bench and tested using the network analyzer to verify its value. The hybrid coupler was tested on the bench using an Agilent 5000 oscilloscope and the HP8751 network analyzer. Port 1 (Tx port) of the hybrid was connected to port 1 of the network a analyzer, the two output ports, Port 2 and Port 3, were connected to the two input channels of the

oscilloscope respectively. The input impedances of the oscilloscope had been previously set to 50Ω . Port 4 (Rx port) of the hybrid coupler was connected to port 2 of the network analyzer. By doing a S21 measurement and setting the central frequency to 127.74MHz with a 0Hz span, we obtained two signals on the oscilloscope having the same amplitude with a 90-degree phase shift.

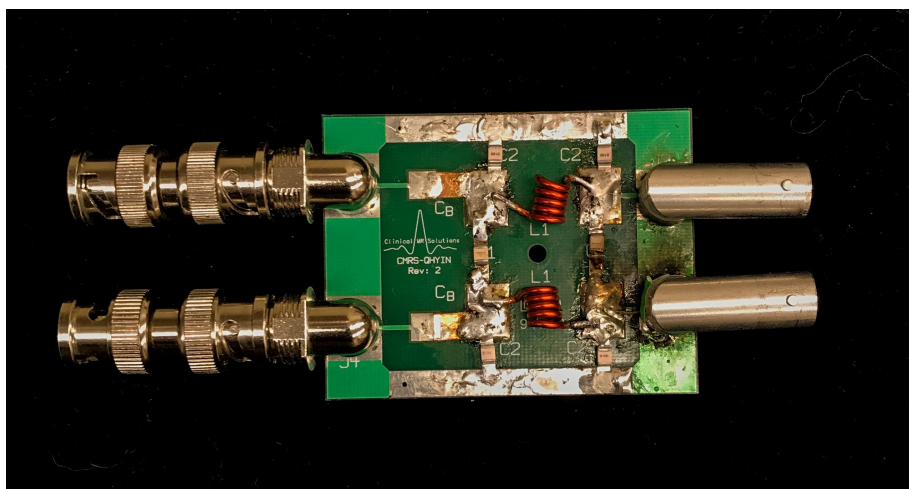


Figure 14: Completed lumped elements of the $\lambda/8$ hybrid coupler.

It is desirable to achieve good isolation between Port 1 (Tx) and Port 4 (Rx) to provide protection to the pre-amplifier during the excitation. The isolation between these two ports was measured with the same configuration, and the span of the network analyzer was set to 20MHz. From the test result we obtained an isolation of -36dB between the Tx and Rx port at the resonant frequency of 127.74MHz.

4.2.4 \vec{B}_1 field mapping and field inhomogeneity calculation

One of the most essential performance measures of a transmit coil is the \vec{B}_1 field homogeneity. There are several NMR techniques that can be used to quantitatively measure and mapping the \vec{B}_1 field [19, 20, 21]. In this work, a technique called the double angle method (DAM) is used [22, 23]. With this method, two RF pulses are applied to excite the magnetization to a flip angle of α and 2α respectively. When a long repetition time ($TR \gg T_1$) between the two scans, the two acquired FID signals S_1 and S_2 can be considered independent of relaxation times, and only proportional to $\sin(\alpha)$:

$$S_1 \propto M_{xy1} = M_0 \sin \alpha \quad (52)$$

$$S_2 \propto M_{xy2} = M_0 \sin 2\alpha \quad (53)$$

By combining (52) and (53), one obtains the value of α :

$$\alpha = \arccos\left(\frac{S_2}{2S_1}\right) \quad (54)$$

It should be noticed that the above calculation is based on the assumptions that the durations of the RF pulses are significantly smaller than T_1 and T_2 , so the relaxation terms in the Bloch equations are ignored, and that M_0 is constant during the RF pulse. This has been demonstrated to be true for small flip angles, and work well for a flip angle up to 90 degrees. [24] At a

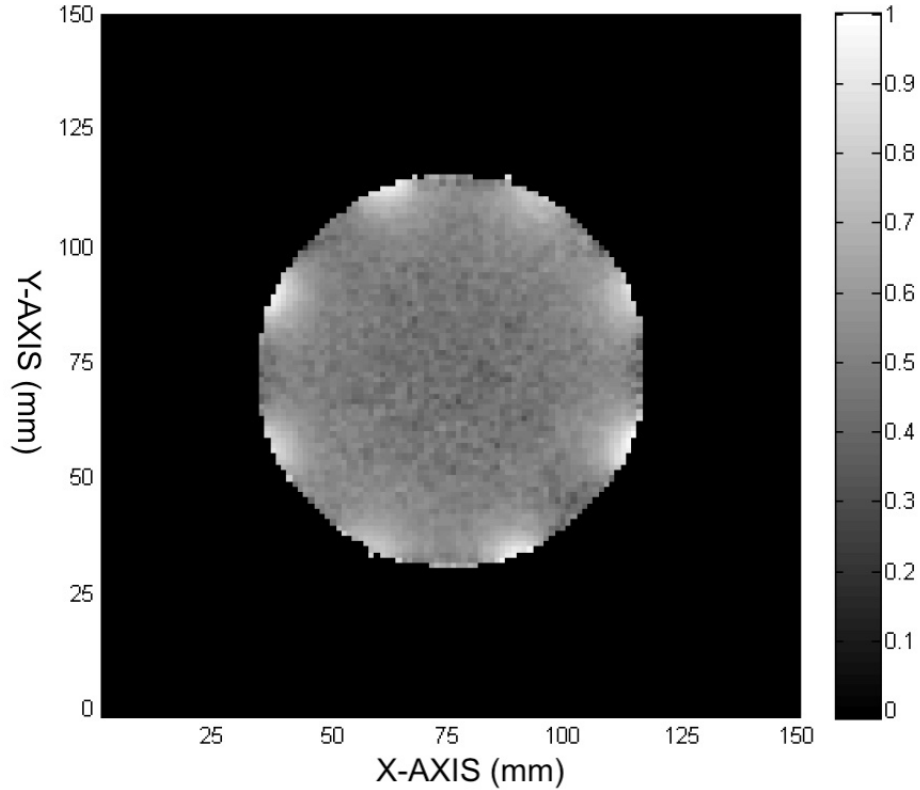


Figure 15: Normalized \vec{B}_1 map of a transverse slice at the centre of the coil.

small flip angle $\vec{B}_1 \propto \alpha$, thus by calculating and generating flip angle maps, one can evaluate the field homogeneity of the coil. The limit of this method is that is inherently slow, since the TR must be long enough to ensure full relaxation of magnetization between two flip angles. This may result in a very long scan time, especially in the case of a long T_1 nuclei.

A balloon was filled with water and placed inside the coil to create a homogeneous spin system inside the coil. The \vec{B}_1 mapping scan was performed

on a 20mm-thick transverse slice at the centre of the coil, with $\alpha = 45$ degrees. The TR was set to be 15s on considering the T_1 of water is 3120ms, thus satisfying the above assumption. The full normalized B_1 map of the built ^1H -transmit birdcage coil is shown in Figure 15. A 4cm x 4cm x 3cm region at the centre of the coil, where the sample will be placed for Rabi measurement, was chosen for a qualitative inhomogeneity study (Figure 16). The average normalized B_1 thorough the entire region was calculated to be 0.8731. with a standard deviation of 0.0426. Therefore the variation of the B_1 field strength at the centre region is about 4.9%.

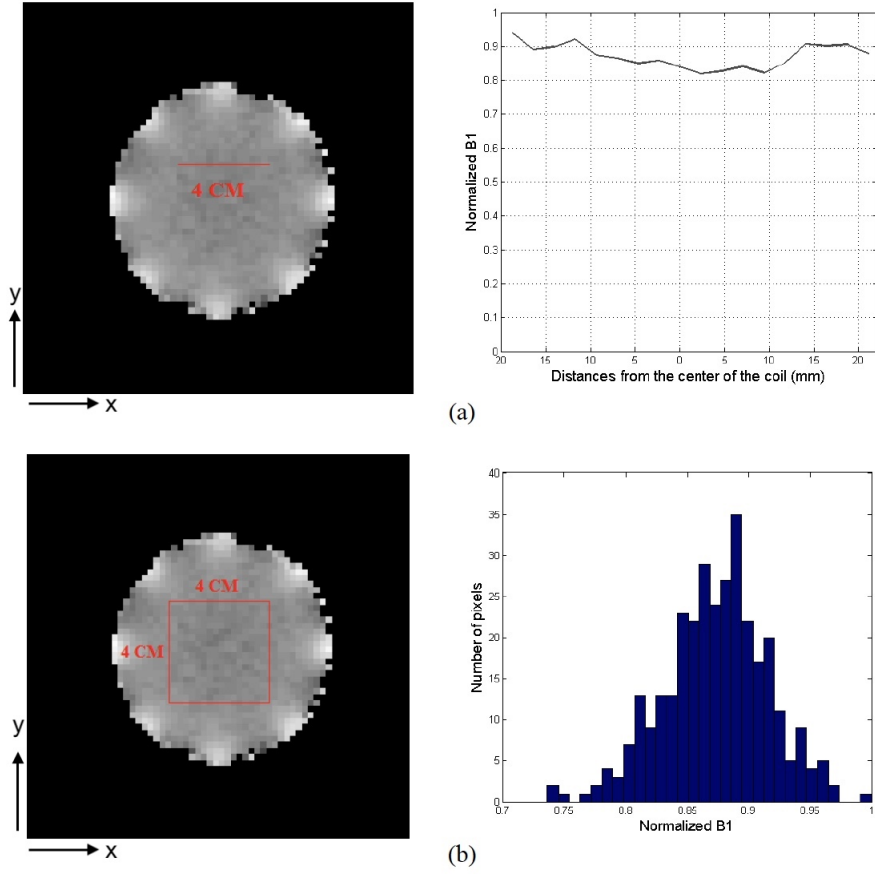


Figure 16: (a) Normalized \vec{B}_1 field distribution in one slice of the map 4cm, and (b) histogram of the normalized \vec{B}_1 field throughout the centre region of the coil.

4.3 Methodology and Circuitry for Detecting Rabi Oscillations

As previously stated in Section 3, acquisition of signal through the clinical scanner cannot be carried out simultaneously with application of \vec{B}_1 thus, stand-alone signal acquisition apparatus is required.

4.3.1 Design Considerations

Since signal detection is to be accomplished through induction, signals will be proportional to the field strengths \vec{B}_1 and the Rabi field, and inversely proportional to the period of each oscillation. The combination will favour the voltage induced through \vec{B}_1 by many orders of magnitude. To address this fundamental obstacle a circuit design is required which can reject the bulk of the induced voltages from \vec{B}_1 . The eventual solution to the problem will be multi-staged.

The first and most important stage is the choice of a parallel LC resonant circuit tuned to the expected Rabi frequency and consequently highly rejective of the \vec{B}_1 voltages. It is estimated that the voltage across an open circuit inductor of only a few turns, from the applied \vec{B}_1 would have been approximately $300V_{pp}$. With the addition of a large parallel capacitance ($\sim 900\mu\text{F}$) this 'tank' circuit should decrease the \vec{B}_1 voltage significantly.

By simulating the tank circuit as outlined in section 4.3.2, it appears that residual \vec{B}_1 voltages will still require further reduction. So half-wave diode

rectification of the output voltage from the tank circuit will be employed to further reduce residual \vec{B}_1 voltages. Due to rectification the output of this stage will now be unipolar which permits low-frequency integration, filtering and amplification of any Rabi signal.

4.3.2 Circuit Simulations

In order to test certain circuit and filter configurations before being built in-lab, circuit simulation software LTSpice was used to simulate circuit output.

The circuit source function is the Thevenin equivalent of the induced voltage in the coil, consisting of a sum of (i) a product of 575Hz (ω_1) and 127.78 MHz (ω_0) sinusoidal waves and (ii) a separate 575Hz (ω_1) sinusoid. This source voltage function is chosen to represent terms in the Bloch equation (36) creating a modulated input voltage of two sinusoidal waves oscillating at ω_0 and ω_1 .

This is then fed to the RLC tank circuit, wherein a small winding resistance R intrinsic to the inductor is included. In the MRI bore, the tank circuit will be the source of induced voltages. The simulation, however, fails to anticipate for the ample amounts of background signal that may be present from power line or RF pickup in the lengthly amounts of cabling ($\sim 15\text{m}$) separating the tank circuit from the remaining circuit stages present outside the magnet room.

Schottky diode rectification of the tank output produces a half-wave rectified signal for forward voltages greater than approximately 0.3V. The signal

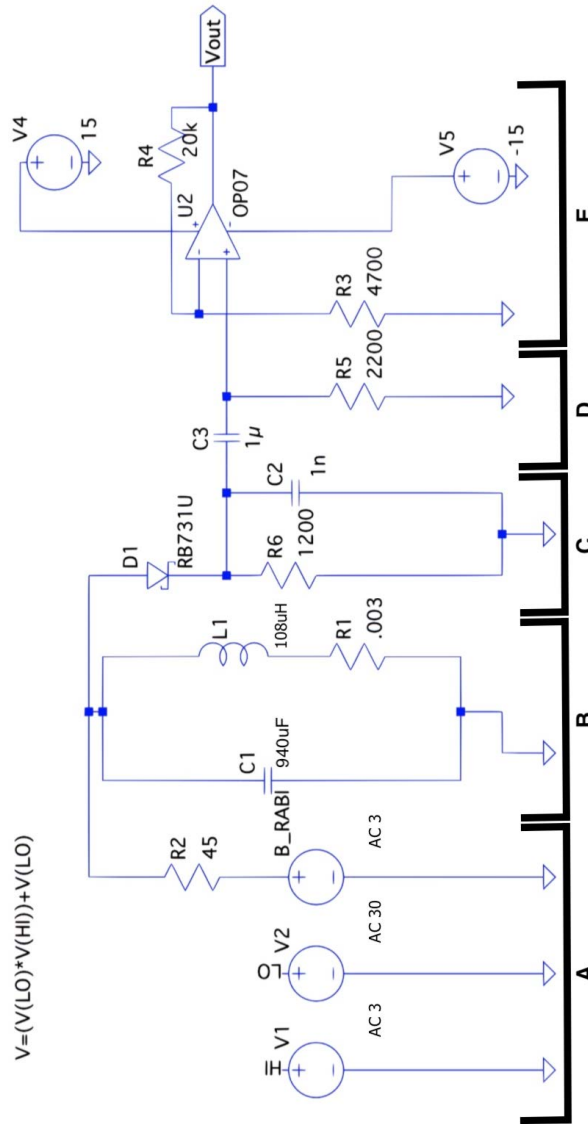


Figure 17: LTSpice Circuit Simulation. The final staged circuit configuration which lead to the simulated output of Figure 18: A. Thevenin equivalent of induced voltage source. B. RLC 'tank' circuit composed of detector coil (Figure 20). C. Half Wave Rectifier and RC integrator. D. High Pass filter to remove DC component of signal. E. Non-inverting amplifier with gain of 5.2.

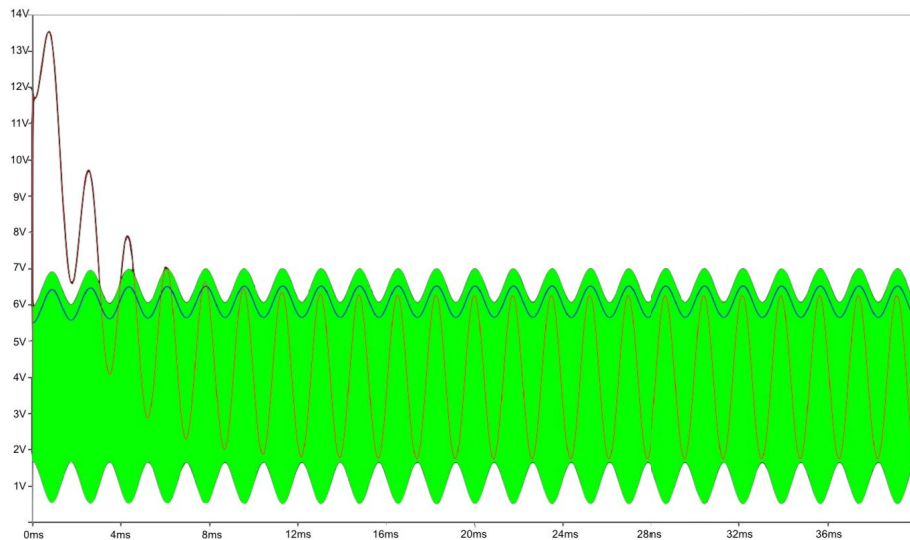


Figure 18: LTSpice Circuit Simulation. A simulation was run where a 3V signal at a carrier frequency of 127.74MHz was modulated with a 0.3V signal oscillating at 575Hz and was simulated for 40ms (green trace). The blue line represents the voltage after the rectification and integration, and the red trace represents the output voltage after amplification.

is then integrated in a parallel RC stage converting the input into a unipolar trace of the modulation envelope with a built in DC offset near the amplitude of the rectified input. Removal of the DC offset required a 'high pass' (with respect to DC) filter with a cut-on frequency of approximately 100Hz. After filtering the voltage output will decay towards a 0V offset determined by the appropriate RC time constant.

Finally the signal is fed into a non-inverting amplifier, with a gain of 5.2 in order to amplify the modulated frequency of interest. This staged design, as depicted in Figure 18, appears to produce a single sinusoidal output at

the modulation frequency (ω_1) with minimal ω_0 voltage.

Figure 18 displays the output of the circuit simulated in Figure 17. The simulation was run for 40ms, and the voltage at various points in the circuit were analyzed to help predict the circuit response. In Figure 18 the green trace represents the input modulated voltage signal, the blue trace represents the voltage signal after rectification and integration, and then final output of the circuit after amplification is represented by the red trace. This circuit successfully removes the high frequency carrier signal while transmitting through the amplified modulation frequency.

4.3.3 Detection Coil Geometry, Tuning, and Matching

Copper wire was wrapped around an acrylic tube to form a tightly wound solenoid for detection of Rabi oscillations (Figure 20). The use of a surface coil ensures maximum coil sensitivity as no information regarding the location of spin origin is required for this work. A clear acrylic tube with a diameter of 3.8cm was wrapped in 16 gauge copper wire for a total of 65 turns with a wire bundle diameter of 14mm.

The series inductance of the coil can be estimated using the following expression derived by Ramo *et al.* [28]:

$$L = Nr^2\mu_0 \left[\ln \left(\frac{16r}{a} \right) - 2 \right] \quad (55)$$

where N is the number of turns in the coil, μ_0 is the permeability of free

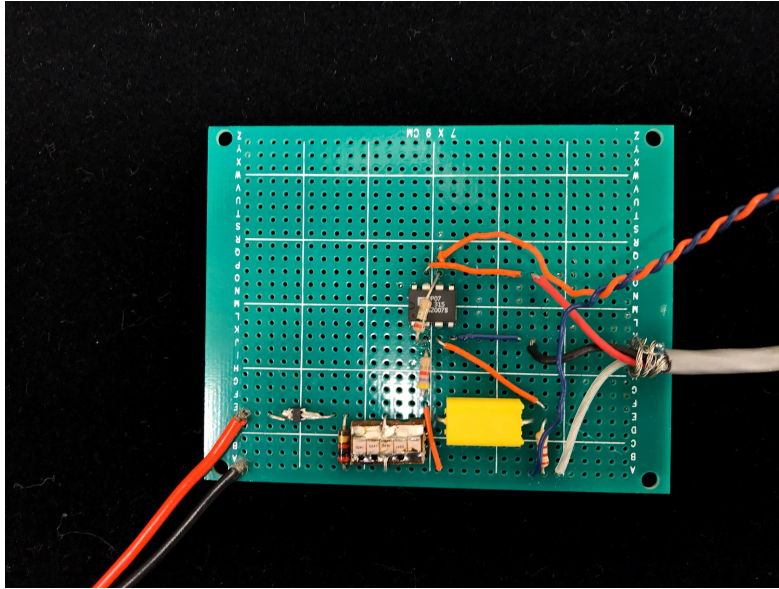


Figure 19: Constructed circuit of Figure 17C, 17D, and 17E.

space, r is the coils radius, and a is the diameter of the wire bundle cross section. For the parameters of the detection coil, an inductance of 0.108mH is found.

In order to tune the detection coil to 575Hz (Frequency of Rabi oscillations in $13.5\mu\text{T}$ field), two $470\mu\text{F}$ capacitors were placed in parallel across the terminals of the coil attached to PCB circuit board. In order to match the coil's impedance to the external transmission line and downstream devices as discussed in section 2.2.2, a secondary matching capacitor was placed in series with the two $470\mu\text{F}$ capacitors.

The resonant frequency of the detection coil was measured using an RF transmit-probe previously tuned to 575Hz on a HP 5353 function generator

where the output frequency was swept from 5Hz to 150MHz. The detection coil connected to an Agilent 5053 oscilloscope where the resonant frequency was measured from the coil's voltage response.

4.3.4 Circuit Construction

Figure 19 and 20 show the constructed circuits from simulations. The first stages of the detection circuit (Figure 17A, 17B) is composed the sample and detection coil (Figure 20) as outlined in section 4.3.3. All circuit elements in Figure 17C, 17D, and 17E were soldered to a PCB circuit board (Figure 19). The first element in the circuit. a RB731U Schottky Barrier Diode was used for its high voltage rating (40V) and high speed switching applications.



Figure 20: The Rabi detection coil. The Rabi detection circuitry outlined in Figure 17B with a 30mL water sample placed inside.

This was then fed to the RC summer circuit composed of one 2000 Ω carbon resistor in parallel with 5 capacitors of an equivalent capacitance of 1nF ($4 \times 240\text{pf} + 1 \times 40\text{pf}$). The choice of the carbon resistor was critical, as analysis of the frequency response of previously used film resistors behaved as inductors at high frequency, thus impairing proper circuit function. The ceramic capacitors used to create the equivalent capacitance of 1nF were high-Q, Low ESR rated, all rated to maintain their capacitive qualities at high frequency.

The high pass filter that followed was composed of a 1 μ F film capacitor and a 2200 Ω film resistor. At this stage in the circuit, the input signal has been transformed from a high-frequency AC voltage to a low-frequency oscillating DC signal, thus the use of film resistors and capacitors is acceptable. The purpose of this filter is to remove the DC offset from the output signal, so a high pass filter with a very low RC constant is used.

The final element in the circuit is a non-inverting amplifier set up with 4700 Ω , and 20,000 Ω film resistors to give a voltage gain of 5.26. The OPO7 was chosen for its reliability, voltage stability, and wide input voltage range. The output was fed directly into a HP 5053 oscilloscope for signal acquisition.

4.4 Experiments

For direct measurements of Rabi oscillations, scans were performed on a Phillips Acheiva 3 Tesla MR Scanner. The in-house built birdcage coil (Section 4.2) used for transmission of the \vec{B}_1 field, was placed with the coil's

axis parallel to the axis of the magnet Bohr (z-axis), and was interfaced to the scanner through the $\lambda/8$ hybrid coupler (Section 4.2.3) connected to the scanner's Dual Frequency Gateway (DFG) interface device. This allowed for the clinical MR scanner to drive the \vec{B}_1 field through the built birdcage coil. The Rabi detection coil, tuned to the expected Rabi frequency was placed in the centre of the birdcage coil. With the axis of the coil aligned with the z-axis of the scanner to most efficiently detect the longitudinal component of the magnetization. The sample under investigation was then be placed in the centre of the detection coil ensuring maximum sensitivity and filling factor to the detection coil.

The output of the detection coil was connected to a micro-coaxial cable and fed through the wave-guide of the scanner room to the outside console room. At this point the cable was fed to the filtration circuit (Figure 19), the output of which was sent to a HP5053 oscilloscope which was triggered on an upwards voltage spike at a value determined well above the noise threshold. The oscilloscope then would record the 1×10^7 points at a rate of 10MSa/s, allowing for sufficient sampling for the full duration of the \vec{B}_1 pulse.

4.4.1 Variation of \vec{B}_1 Amplitude

It is suggested by (45) that the voltage induced in the coil consists of three components, however for our measurement of Rabi oscillations we are only interested in $V_{\omega_1, SAMPLE}$. To validate our results as representing the Rabi components, an experiment is proposed in which the amplitude of the applied



Figure 21: MRI Experiment Set Up. The Birdcage coil used to produce the B_1 field is placed in the centre of the magnet and connected to the $\lambda/8$ hybrid coupler which is then fed to the DFG of the scanner. The detection coil is placed in the centre of the birdcage coil with its output being fed through an interface to outside the scanner room to the filter circuit (Figure 19) and then to an oscilloscope where data is recorded and visualized.

\vec{B}_1 field is varied. In doing so, the expectation is that the frequency of the measured Rabi signal should scale accordingly with (37). A reference \vec{B}_1 of $13.5\mu\text{T}$ will first be tested, chosen to match the clinically used \vec{B}_1 on this scanner. Two additional \vec{B}_1 amplitudes of half and double the reference amplitude will be used respectively.

Control of the \vec{B}_1 field through the scanner's software is done through setting both the \vec{B}_1 amplitude (B_1) and flip angle α . The maximum allowable flip angle through manipulation the scanner's software being $30,000^\circ$. The

pulse duration (τ) can be found from rearranging (70):

$$\tau = \frac{\alpha}{\gamma B_1} \quad (56)$$

With α being kept constant through each \vec{B}_1 , τ will change inversely-proportional to the change in \vec{B}_1 . The three B_1 amplitudes of 6.75T, 13.5T, and 27T result in will have pulse durations of 289.9 ms, 144.9ms, and 72.49ms respectively. The corresponding Rabi oscillations are expected to be observed at frequencies of 287.5Hz , 575Hz, and 1150Hz. For all trials a 30mL sample ($N = 9.79 \times 10^{23}$) was used.

4.4.2 Dependency on Number of Nuclei

To further verify behaviour of Rabi oscillations within a spin system, the next goal is to show that the signal strength of the detectable Rabi oscillation varies with the amount of nuclei in the sample, verifying (28). To do this, water sample sizes of 30mL , 15mL and 0mL were exposed to an applied \vec{B}_1 of $13.5\mu\text{T}$ with α remaining constant at $30,000^\circ$. Neglecting the minor changes in filling factor and loading of the coil, (27) suggests that signal scales proportionally with N , as the total magnetization in (38) $M_{xy}(\vec{r})$ will increase proportionally.

4.4.3 RF Coil Field Calibration

To determine if the magnitude of the measured Rabi oscillations can be applied to nanotechnology, the strength of the oscillating magnetic field must be determined.

In order to determine the strength of this field, the principle of reciprocity will be used. The reciprocity principle with respect to MR signal states that when the RF coil is used as a receiver to measure an arbitrary current density, flux is created through the coil. For the same coil to transmit that same current density, the same flux through that coil must be produced. In summary, any induced voltage in the coil due to an oscillating field of a set strength will be the same.

To calibrate the coil, an oscillating magnetic field at 575Hz will be generated by a in-house built Helmholtz pair (Figure 23). Each coil in the Helmholtz pair was constructed with 130 turns of 18g copper wire with a radius of 0.0525m, a coil pack length of 0.02m, and coil pack thickness of 0.006m. The coil pair was separated by a distance equal to the radius of the coils.

The RF detection coil was then placed in the centre of the Helmholtz pair, with the coil axis being parallel to the axis of the pair. The pair was connected to an oscilloscope so that the frequency of oscillation of the field could be monitored. To control the field strength generated by the Helmholtz pair the current passed through the coils was varied from 100mA to 1000mA. The field strength measured by a Pacific Scientific OECO Gauss Meter at the centre

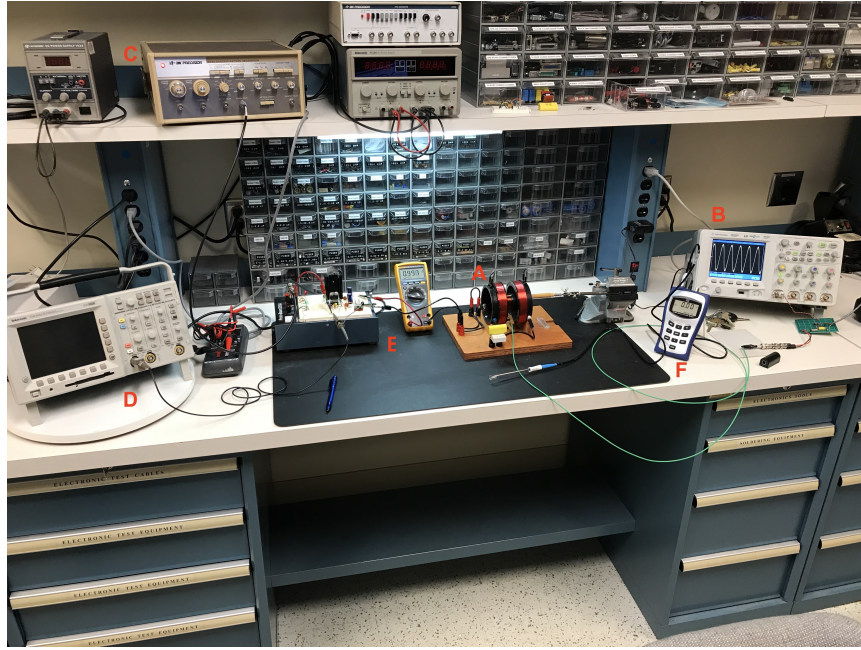


Figure 22: RF Coil Calibration Setup. Helmholtz pair (A.) set up oscillating at 575Hz, with an AC function generator (C.) which permits current through the coil to be varied. RF Detection coil (A) is placed in the centre of the Helmholtz pair and hooked up to the filtration circuit and oscilloscope (B) to measure induced voltage.

of the detection coil produced by the Helmholtz pair. These values were then compared to the calculated field values from the theoretical expression for magnetic field of a Helmholtz pair derived from the Biot-Savart law [29]

$$B_z = \left(\frac{4}{5}\right)^{3/2} \frac{\mu_0 N I}{R} \quad (57)$$

The detection coil was connected to the filter circuit used in the MR measurements to ensure accuracy in the calibration, and then fed to an oscilloscope

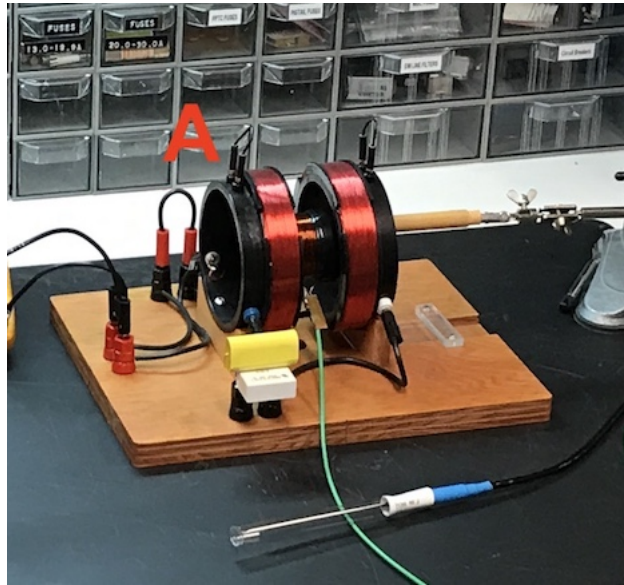


Figure 23: Scaled view of Figure 22A. The Rabi detection coil placed along the z-axis of the Helmholtz pair, simulating the experimental setup within the MRI. The Gauss meter (bottom) was then placed inside the coil to measure the magnetic field.

where the induced V_{pp} was measured. From here the relationship between induced V_{pp} in the coil and B-field can be determined and used for comparison with results to estimate the strength of the Rabi field.

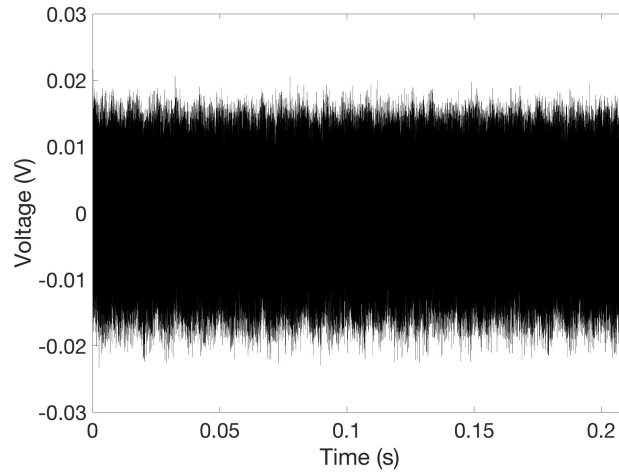


Figure 24: Signal during the application of a \vec{B}_1 of $6.75\mu\text{T}$

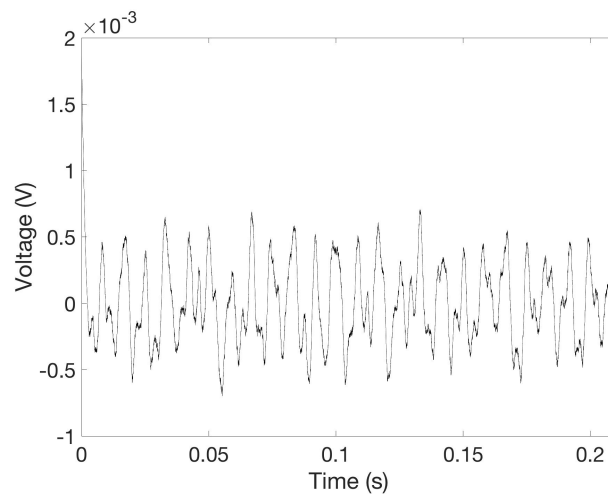


Figure 25: Savitzky-Golay filtered signal during the application of a \vec{B}_1 of $6.75\mu\text{T}$. This data is the filtered result of Figure 24.

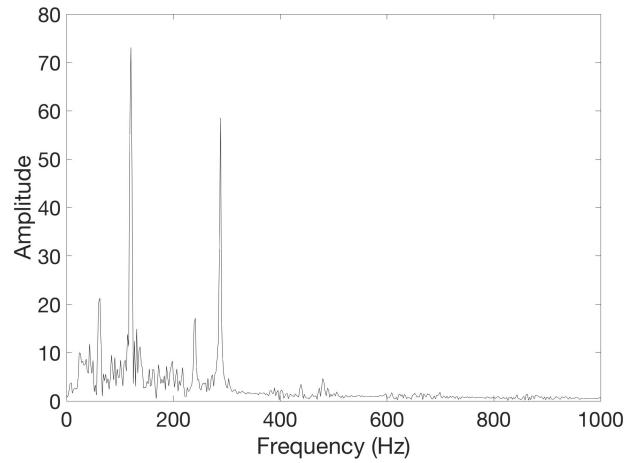


Figure 26: Fourier transformed signal during the application of a \vec{B}_1 of $6.75\mu\text{T}$. This is the Fourier transform of the data seen in Figure 25. A main Frequency component due to Rabi oscillations can be viewed at 288.2Hz.

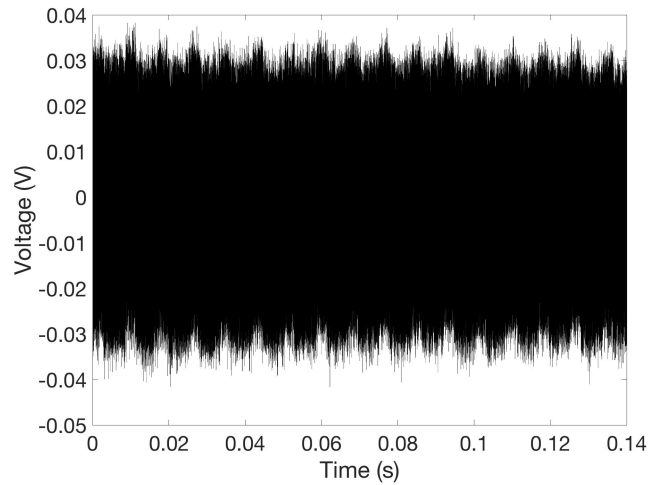


Figure 27: Signal during the application of a \vec{B}_1 of $13.5\mu\text{T}$

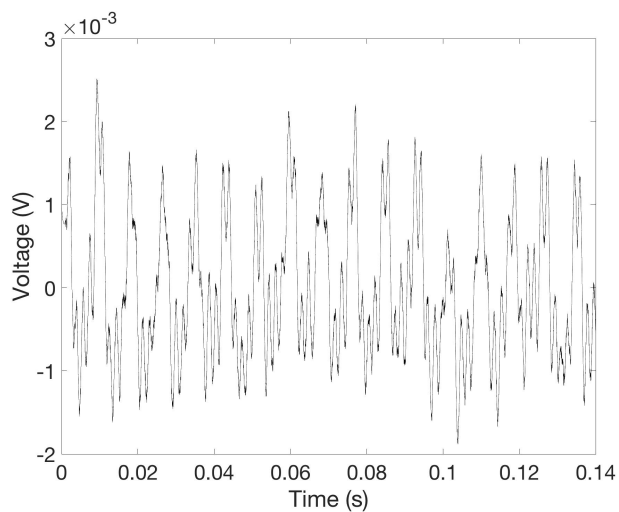


Figure 28: Savitzky-Golay filtered signal during the application of a \vec{B}_1 of $13.5\mu\text{T}$. This data is the filtered result of Figure 27.

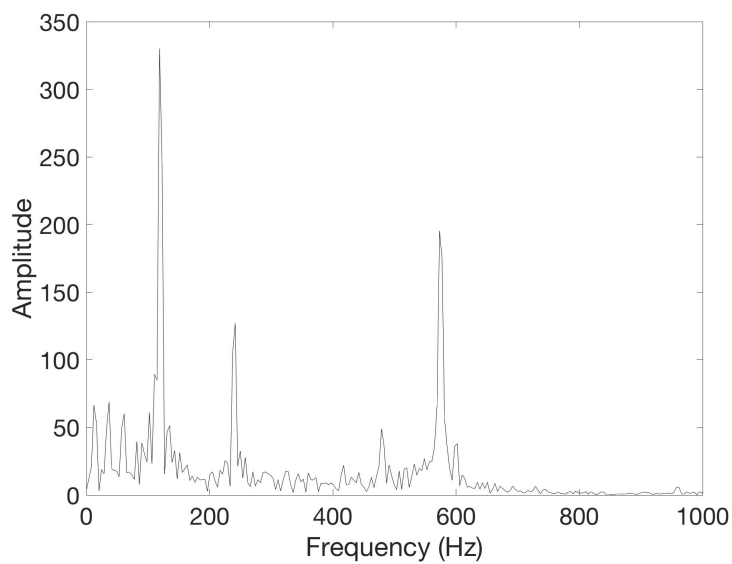


Figure 29: Fourier transformed signal during the application of a \vec{B}_1 of $13.5\mu\text{T}$. This is the Fourier transform of the data seen in Figure 28. A main Frequency component due to Rabi oscillations can be viewed at 573Hz.

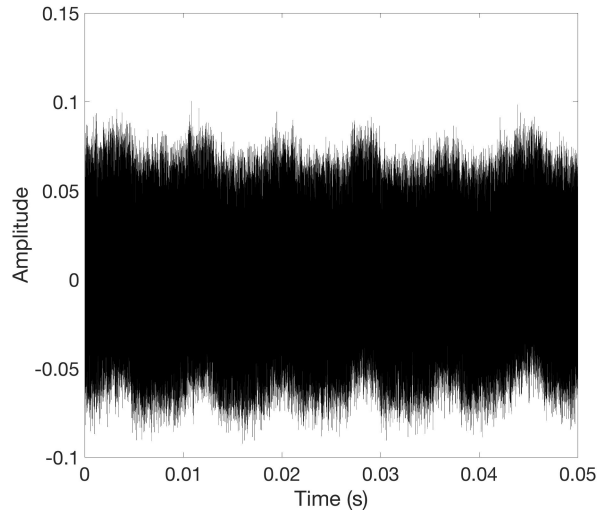


Figure 30: Signal during the application of a \vec{B}_1 of $27\mu\text{T}$

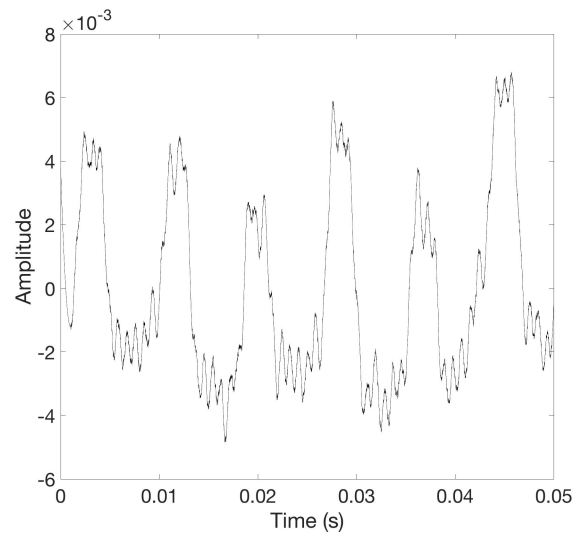


Figure 31: Savitzky-Golay filtered signal during the application of a \vec{B}_1 of $27\mu\text{T}$. This data is the filtered result of Figure 30.

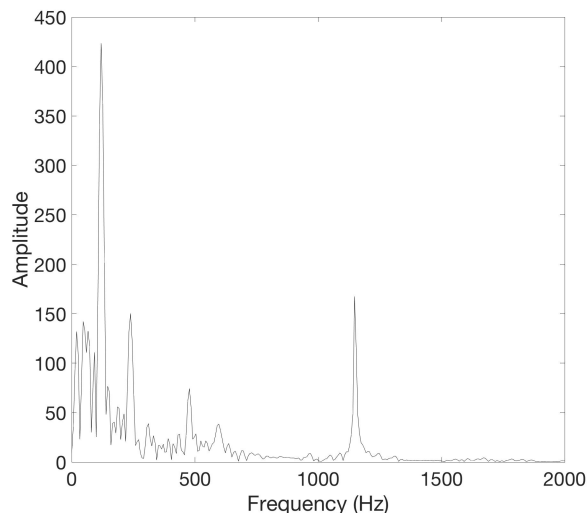


Figure 32: Fourier transformed signal during the application of a \vec{B}_1 of $27\mu\text{T}$. This is the Fourier transform of the data seen in Figure 31. A main Frequency component due to Rabi oscillations can be viewed at 1147Hz.

4.5 Results

The initial measurement of Rabi oscillation was conducted with an applied B_1 of $13.5\mu\text{T}$, resulting in the signal found in Figure 27. This signal was then filtered using a Savitzky-Golay (SG) smoothing filter (Figure 28), in order to reduce the amount of noise without distorting the signal. The filtered signal was then Fourier Transformed revealing the various frequency components in the signal (Figure 29). A main peak was observed at 575Hz, the expected Rabi frequency. To confirm the origin of this signal being the result of Rabi oscillations, subsequent experiments are discussed in this section.

4.5.1 Variation of \vec{B}_1 Amplitude

Figure 24 through Figure 32 shows series of signals from various applied \vec{B}_1 -field amplitudes. For each acquisition the flip angle (α) was kept constant at the maximum allowed value of $30,000^\circ$, leading to varying pulse duration times for each B_1 . Figures 24, 27 and 30 display the raw voltage signals during the application of each respective B_1 field. Direct analysis of this signal is made difficult by low SNR, thus signal filtration is utilized.

These datasets were then put through a SG smoothing filter. The SG filter is a common digital filter used to smooth datasets, and increases the SNR of a dataset without greatly distorting the dataset. The SG filter fits successive sub-sets of adjacent data points to a low degree polynomial. For the purpose of these datasets the SG MatLab filter of fourth order was applied. This greatly reduced the amount of noise within the signal, allowing for major frequency components to be visualized. Comparing the SNR from peaks due to filtered and unfiltered signal, a 100 fold increase in SNR is observed. Figures 25, 28 and 31 display the filtered datasets for each respective B_1 .

The filtered datasets were subsequently passed through a discrete Fourier transform using MatLab's 'fft' function. This technique allows for analysis of the main frequency components present within the signal. Figures 26, 29, and 32 display the Fourier transformed signal for each applied B_1 .

Analysis of the frequency components from signals of various applied B_1 field's displays a constant peaks at 120Hz, 240Hz, and 480Hz. The signals from an applied B_1 fields of $6.75\mu\text{T}$, $13.5\mu\text{T}$, and $27\mu\text{T}$ each display unique

peaks at 288.2Hz, 573Hz, and 1147Hz respectively.

4.5.2 Dependency on Number of Nuclei

Figure 33 displays the Fourier transformed signal from an applied B_1 of $13.5\mu\text{T}$ of constant duration with varying sample sizes. All raw signal was put through the same signal smoothing and Fourier analysis as outlined in 3.6.1. The SNR of signal due to Rabi oscillating magnetization at 575Hz was then calculated for each of the three sample sizes. For sample sizes of 30mL and 15mL SNR's of 772.94, and 326.47 were calculated. For the 0mL sample spectra, no distinguishable peak can be observed and thus has an SNR of 0.

Table 1: RF Detection Coil Field Calibration (575Hz)

Current (A)	Calculated Field (μT)	Measured Field (μT)	Induced Voltage (V_{pp})
0.1	222.6	223	0.888
0.2	445.2	447	2
0.3	667.8	670	2.75
0.4	890.4	893	3.44
0.5	1113	1117	4.13
0.6	1335.6	1340	4.84
0.7	1558.2	1561	5.38
0.8	1780.8	1780	6.03
0.9	2003.4	2005	6.63
1.0	2226	2230	7.25

4.5.3 RF Coil Field Calibration

As various currents were supplied to the Helmholtz pair the produced field was measured with the use of the Gauss meter as shown in Figure 23 and

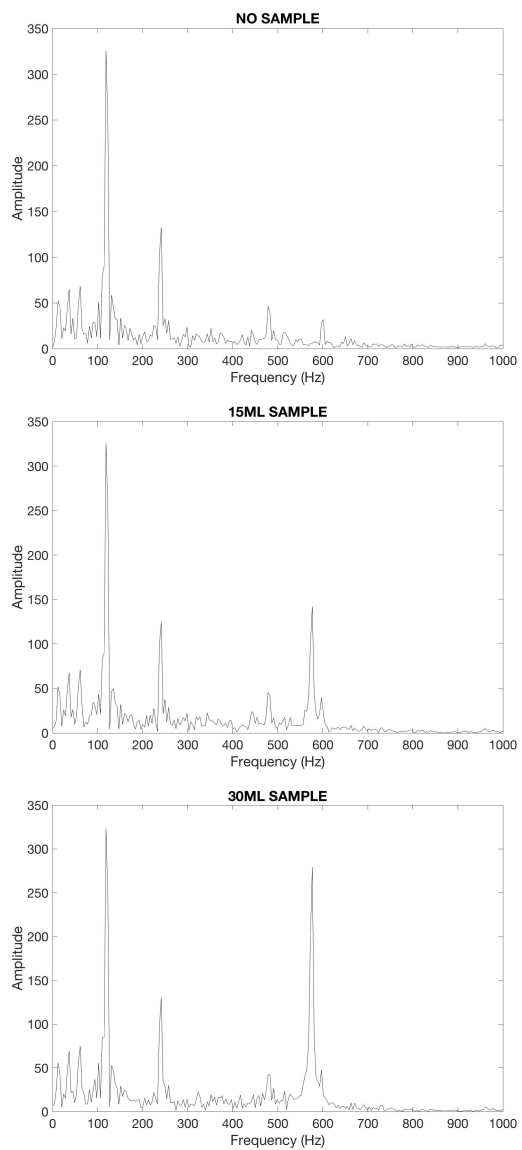


Figure 33: Rabi Oscillations with varied sample size. Signal spectra from an applied \vec{B}_1 field of $13.5\mu\text{T}$ with sample sizes of 0mL (top), 15mL (middle), and 30mL (bottom).

compared to the calculated value from (57). For each of the three applied field strengths, the induced peak-to-peak voltage (V_{pp}) was measured (Table 1). To then find the dependency between the induced voltage in the detection coil and applied magnetic field, the induced voltage is plotted as a function of calculated field and fitted linearly (Figure 34). The linear fit yielded a constant of proportionality of 3438.2.

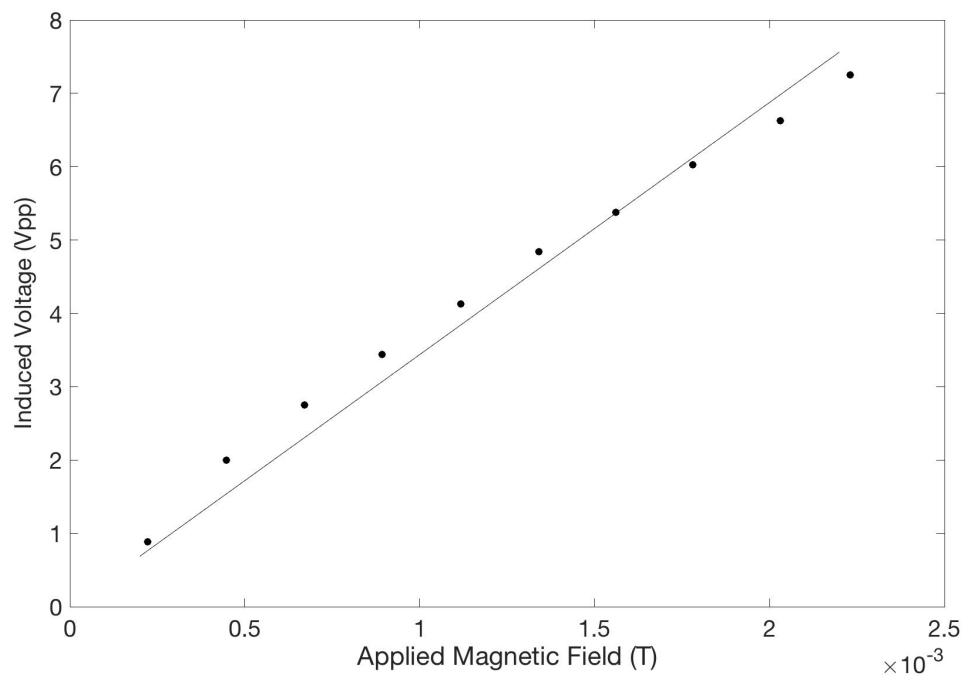


Figure 34: RF Detection Coil Calibration

4.6 Discussion

4.6.1 Variation of \vec{B}_1 Amplitude

Through filtering and Fourier analysis of raw signal as outlined in 3.6.1, an observable peak at 573Hz is detected from an applied B_1 of $13.5\mu\text{T}$. The theoretically predicted Rabi frequency from (37) of 575Hz is in excellent agreement with this measured value. This finding is believed to be the first direct measurement of Rabi oscillations in a nuclear spin system.

To verify that the observed oscillations were indeed due to Rabi oscillations, the \vec{B}_1 amplitude was then varied. When a \vec{B}_1 field with amplitude of $6.75\mu\text{T}$ was applied, a main frequency component is visible at 288.2Hz which is in excellent agreement with the predicted value from (37) of 287.5Hz. A \vec{B}_1 field of $27\mu\text{T}$ was then applied to the sample in which a main frequency component in the signal is visible at 1147Hz again close to the very expected value from (37) of 1150Hz.

The success of this measurement is largely attributable to the circuit described in 3.4. With only the tuned tank detector in place, the oscilloscope measures a $40V_{pp}$ sinusoidal signal oscillating at ω_0 (128MHz). The conditioning reduces this overpowering signal to hundreds of millivolts.

Demonstrating the shift of the detected Rabi frequency with the change in strength of applied \vec{B}_1 verifies the claim that the origin of this signal in this work is due to the Rabi oscillation.

A notable result of these experiments is the narrow line width of the Rabi

peak. When compared to the monotonic signal of the 120Hz peak, the Rabi peak which is due to nuclear oscillations of millions of nuclei is similarly narrow, and is a consequence of the homogeneity of the excitation field as described in section 4.2.4.

4.6.2 Dependency on Number of Nuclei

To further the investigation into the Rabi field, it is important to demonstrate that the strength of this field depends on the number of nuclei present within the volume being excited. The results of (27) and (38) imply that the magnetization varied linearly with N , meaning that the total magnetization available to undergo a Rabi Oscillation also varied with N .

With an applied B_1 of $13.5\mu\text{T}$ to the water sample, the expected Rabi frequency is visible with a peak in the frequency spectra at 573Hz. Figure 33 displays the frequency spectrum from various sample sizes of 30mL, 15mL and 0mL. No Rabi signal was observed from the 0mL sample, which has two-fold implications, that the previously observed signal as discussed in 4.6.1 must be originated from the sample volume itself, and that without N nuclei present within the sample, no Rabi oscillations are observed in agreement with (38). Spectra from 15mL and 30mL samples of water displayed visible peaks at the expected Rabi frequency.

Comparing the SNR of the signal peaks from the two samples, signal from the the 30mL sample had 2.36 times signal strength of the 15mL sample at SNR's of 772.94 and 326.47 respectively. The variance in the expected factor

of two can be attributed to differences in loading of the detection coil and filling factor as outlined in 1.4.8. With this agreement in volumetric results, it can be seen that the strength of signal due to Rabi oscillations varies linearly with N .

4.6.3 RF Coil Field Calibration

It is important for this work to not only demonstrate that these Rabi oscillations are detectable, but to provide quantitative characterization of the strength of the magnetic field created by these oscillations. By creating an oscillating magnetic field at a known B -amplitude and finding the corresponding induced voltage in our measurement system, it is possible to determine the linear correlation between applied B_1 and induced voltage in the detection coil. By varying the current supplied to the Helmholtz pair, various field strengths are produced. By comparing the measured field values against the theoretical values from (37) it can be seen (Table 1) that the produced field is linear across the tested range. The Helmholtz pair was used to create oscillating fields between $222.6\mu\text{T}$ and $2226\mu\text{T}$ in order to obtain a wide range of induced voltages. When the detection coil was placed inside the Helmholtz pair, the induced voltages created by the various field strengths was measured, and then plotted for analysis (Figure 34). A linear fit resulted in a proportionality constant between induced voltage and applied magnetic field of 3438.2. Taking this result we can conclude that:

$$V_{pp} = 3438.2 \times B \quad (58)$$

this permits the strength of the field due to Rabi oscillations to be determined by measuring the V_{pp} induced in the coil. However, the induced voltage in the detection coil is composed of multiple frequency components. In order to determine the induced V_{pp} due to Rabi oscillations, the average V_{pp} from the Rabi oscillating signal was measured using filtered spectra (Figures 24, 27, and 30) resulting from various applied B_1 field amplitudes. For the reference B_1 of $13.5\mu\text{T}$, the average induced voltage was determined to be 0.613mV_{pp} .

As the calibration measurement was only conducted at 575Hz, an adjustment to the linear factor in (58) is made to accommodate frequencies of 287.5Hz and 1150Hz. Through the use of Faraday's law (41), it can be seen that through keeping a constant B and through varying dt there is an inverse change in the calibration factor of $\frac{1}{2}$ and 2 for frequencies of 287.5 Hz and 1150 Hz respectively. This can be similarly deduced from (38) where a linear voltage dependency on frequency is seen. This creates a linear correlation factor between V_{pp} and B of 1,719.1 and 6,876.4 for 287.5Hz and 1150Hz respectively.

Furthermore, measurements of 287.5Hz and 1150Hz Rabi oscillating magnetic fields were made using the Rabi detection coil as outlined in section 4.3.3 tuned to a resonant frequency of 575Hz. However, because of the copper wire resistance in the coil, the voltage response of the circuit is broadened enough

to detect the lower 287.5Hz and 1150Hz Rabi signals. To correct for the Q variation however, the response curve was determined (Appendix H). The voltage response at the 3 Rabi frequencies was determined by measuring the relative amplitude at each frequency, normalized to the maximum response near 575Hz.

For applied B_1 of $6.75\mu\text{T}$ and $27\mu\text{T}$ average induced voltages were measured to be 0.35mV_{pp} and 0.9mV_{pp} respectively. Correcting for both change in Faraday induction due to frequency and the voltage-frequency response of the detection coil, corrected voltages for $6.75\mu\text{T}$ and $27\mu\text{T}$ were corrected to be 0.861V and 0.889V respectively. Taking these corrected induced voltage values and using (58), the strength of Rabi field can be calculated as seen in Table 2. It can be seen that the Rabi field strength is determined to be between 250nT , 178nT and 258nT for respective applied B_1 of $6.75\mu\text{T}$, $13.5\mu\text{T}$, and $27\mu\text{T}$.

This preliminary result demonstrates relative consistency in strength of the induced Rabi field across the range of applied B_1 fields. With the sample size (N) being kept constant through each sequential B_1 there is no change in the net nuclear magnetization of the sample, and thus no change in Rabi field strength is expected. This result is in agreement with (28) predicting that constant magnetization should be observed with all other factors kept constant. The small variation between the the Rabi field measurements may be due to off-resonant coil measurements at 287.5Hz and 1150Hz. An average Rabi field strength of $228.67\mu\text{T}$ is found, such field could be a possible

Table 2: Rabi Field Calculation

$B_1(\mu\text{T})$	Induced Voltage (mV _{pp})	Corrected Voltage (mV _{pp})	B _{RABI} (nT)
6.75	0.35	0.861	250
13.5	0.613	0.613	178
27	0.9	0.889	258

candidate for future nanoparticle applications.

4.6.4 Computer Calculation of Rabi Field Strength

In order to verify our determination of the field-strength of Rabi oscillations, a MatLAB code was created to provide a theoretical estimate of the strength of the magnetic field due to a similarly modelled distribution of nuclear spins.

An atomic nucleus effectively acts as a tiny current loop (dipole), and thus we can employ the Biot-Savart Law [29] to calculate the magnetic field at a point due to the dipole using:

$$B_{dip}(r) = \frac{\mu_0}{4\pi} \frac{1}{r^3} [3(\vec{m} \cdot \hat{r})\hat{r} - \vec{m}] \quad (59)$$

which can be rewritten as:

$$B_{dip}(r) = \frac{\mu_0 M}{4\pi} \frac{1}{r^3} (2\cos\theta\hat{r} - \sin\theta\hat{\theta}) \quad (60)$$

By then creating a cylindrical matrix of nuclei spaced at the same concentration of water as used in experiments, an analytical volume integral was calculated by summing the result of (60) across all nuclei relative to a point

on the detection coil.

Modelling a cylinder of water nuclei with a radius of 2cm, length of 4cm, and a concentration of 2.057×10^{-5} mol/m³ matched the experimental setup. By then summing the magnetic field due to each nuclei within the sample to the same point on the detection coil 2.05cm out radially from the cylinder's axis, an estimated magnetic field was determined to be 86.855nT. This preliminary calculation is within a factor of two of the experimentally determined value of 178nT from Section 4.6.3. It is believed that this strength of oscillating magnetic field would be adequate for nanoparticle manipulations. Further studies working with varying chemical species should be undertaken to better understand and characterize this field.

5 Conclusion

This work detected and measured the strength of a Rabi oscillating field for a nuclear spin system, this result has not been previously reported in the literature. Due to the presence of this oscillation only during application of the radio-frequency field, its detection was complicated by the overpowering strength of the applied RF field which is orders of magnitude greater than signal due to Rabi oscillations. In order to mitigate the overpowering signal from the applied RF field, several signal conditioning stages were required for detection of these oscillations. The linear dependencies of the detected Rabi oscillation frequency with respect to strength of the applied RF field, and sample size were validated. The strength of the Rabi oscillating magnetic field was determined to be 173nT at the point of the detection coil for a \vec{B}_1 amplitude of $13.5\mu\text{T}$, this result is in close agreement with theoretical calculations. This 'Rabi field' could be a valid candidate for actuation of biomedical nanoparticles.

References

- [1] K. J. Layton, B. Tahayori, I. M.Y. Mareels, P. M. Farrell, L. A. Johnston *Rabi resonance in spin systems: Theory and experiment* Journal of Magnetic Resonance 242 (2014) 136:142
- [2] R. Glenn, M. E. Limes, B. Pankovich, B. Saam, M. E. Raikh *Magnetic resonance in slowly modulated longitudinal field: Modified shape of the Rabi oscillations* PHYSICAL REVIEW B 87, 155128 (2013)
- [3] B. Tahayori, L. A. Johnston, K. J. Layton, P. M. Farrell, I. Mareels *Solving the Bloch Equation With Periodic Excitation Using Harmonic Balancing: Application to Rabi Modulated Excitation* IEEE TRANSACTIONS ON MEDICAL IMAGING, 34(10), 2015
- [4] A. Kargol, L. Malkinski and G. Caruntu *Biomedical Applications of Multiferroic Nanoparticles*. Advanced Magnetic Materials (2012); 89-118.
- [5] H. S. Huang, J. F. Hainfeldx *Intravenous magnetic nanoparticle cancer hyperthermia*. International Journal of Nanomedicine 2013:8 2521?2532
- [6] A. Seki, E. Kita1, D. Isaka, Y. Kikuchi, K.Z. Suzuki, A. Horiuchi, M. Kishimoto , H. Yanagihara, T. Oda, N. Ohkohchi, H. Ikehata, I. Nagano *Study of the heating characteristics and mechanisms of magnetic nanoparticles over a wide range of frequencies and amplitudes of an alternating magnetic field*. Journal of Physics: Conference Series 521 (2014) 012014

- [7] S. Nappini, M. Bonini, F. Baldelli, F. Pineider, C. Sangregorio, P. Baglioni, B. Norden *Controlled drug release under a low frequency magnetic field: effect of the citrate coating on magnetoliposomes stability*. *Soft Matter*, 2011, 7, 1025-1037.
- [8] J. Corchero, A. Villaverde *Biomedical applications of distally controlled magnetic nanoparticles*. *Trends in Biotechnology* 2009, 27(8); 468-476
- [9] N. A. Usov, B. Y. Liubumov *Magnetic nanoparticle motion in external magnetic field*. *Journal of Magnetism and Magnetic Materials* 385(2015) 339-346
- [10] J. Estelrich, E. Escribano, J. Queralt, M. Busquets *Iron Oxide Nanoparticles for Magnetically-Guided and Magnetically-Responsive Drug Delivery* *Int. J. Mol. Sci.* 2015, 16, 8070-8101
- [11] F. Bloch. M. F. Kircher, M. Koch, L. Eliasson, S. Goldberg, E. Renstro. *Nuclear Induction* *Phys Rev.*, 70:460-473, 1946.
- [12] I. I. Rabi *Syace Quantization in a Gyating Magnetic Field* *Phys. Rev.* 51, 652-654 (1936)
- [13] Feynman et al. *Lectures on Physics Vol. 2* Reading, Mass. :Addison-Wesley Pub. Co., 1963-1965.
- [14] H.D.W. Hill. *Limits of Measurement in Magnetic Resonance*. *J. Phys. E. Sci. Instrum.*, 1:977-983, 1968.

- [15] C. E. Hayes *An efficient, highly homogenous radiofrequency coil for wholebody NMR imaging at 1.5 T* Journal of Magnetic Resonance, (63): 622-628; 1985.
- [16] C.L. Chin and M.B. Smith *Circular and elliptical birdcage coil design for magnetic resonance imaging* , New York: IEEE, 1998.
- [17] C. L. Chin et al. *BirdcageBuilder: Design of specified-geometry birdcage coils with desired current pattern and resonance frequency* , Concepts in Magnetic Resonance, 15(2): 156-163, 2002.
- [18] R. K. Mongia, I.J. Bahl, P. Bhartia, J. Hong. *RF and Microwave Coupled-Line Circuits*. Artech House, Incorporated, 2007.
- [19] Oh C, Hilal S, Cho Z, and Mun I. *Radio frequency field intensity mapping using a composite spin-echo sequence*. Magn Reson Imaging 1990; 8:21-25.
- [20] Morrell GR. *A phase-sensitive method of flip angle mapping*. Magn Reson Med 2008; 60:889-894.
- [21] Sacolick LI, Wiesinger F, Hancu I, and Vogel MW. *B1 mapping by Bloch-Siegert shift*. Magn Reson Med 2010; 63:1315-1322.
- [22] Insko E and Bolinger L. *Mapping of the radiofrequency field*. J Magn Reson A 1993; 103:82-85.
- [23] Hornak JP, Szumowski J, and Bryant RG. *Magnetic field mapping*. Magn Reson Med 1988; 6:158-163.

- [24] Pauly J, Nishimura D, and Macovski A. *A k-space analysis of small-tip-angle excitation*. J Magn Reson 1989; 81:43-56.
- [25] J. Estelrich, E. Escribano, J. Queralt, M. Busquets *Iron Oxide Nanoparticles for Magnetically-Guided and Magnetically-Responsive Drug Delivery* Int. J. Mol. Sci. 2015, 16, 8070-8101
- [26] A. Kargol, L. Malkinski, G. Caruntu, *Biomedical Applications of Multiferroic Nanoparticles* Materials Chem. and Phys. 124(2-3) (2010) 1188-1192
- [27] J. Dobson *Nanomagnetic actuation: remote control of cells* Nature Nanotechnology 3 (2008) 139-143
- [28] Ramo, S., Whinnery, J. R., Van Duzzer, T., Fields *Waves in Communication Electronics*, Wiley and Sons, New York, 1965
- [29] I.S. Grant, W.R. Phillips, *Electromagnetism* (2nd Edition), Manchester Physics, John Wiley and Sons, 2008

Appendices

A The Rotating Frame of Reference

The equation of motion for \vec{M} when an RF excitation field is applied in the presence of a static field now becomes:

$$\frac{d\vec{M}}{dt} = \gamma \vec{M} \times (\vec{B}_0 + \vec{B}_1) \quad (61)$$

The resulting precession of the bulk magnetization is shown in Figure 35.

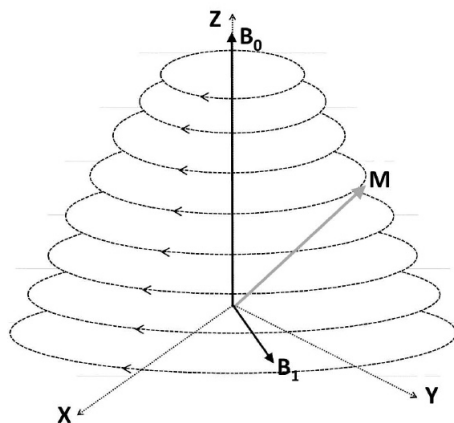


Figure 35: Precession of the bulk magnetization, \vec{M} , in the laboratory frame of reference.

Viewed in the laboratory frame of reference, the precession of the bulk magnetization can now be seen as a spiral path. If however the bulk magnetization is viewed from the frame of reference which is rotating at the Larmor

frequency the precession can be viewed simply as a tipping motion. The definition of the coordinates of the rotating frame are denoted by x' , y' , z' compared to the coordinates of the stationary laboratory frame given by x , y , z . Consider the unit vectors of this coordinate system \hat{x} , \hat{y} , and \hat{z} in any of the three dimensions rotating with angular velocity ω_{rf} then:

$$\begin{aligned}\frac{d\hat{x}}{dt} &= \omega_{rf} \times \hat{x} \\ \frac{d\hat{y}}{dt} &= \omega_{rf} \times \hat{y} \\ \frac{d\hat{z}}{dt} &= \omega_{rf} \times \hat{z}\end{aligned}\tag{62}$$

Assuming a time dependant vector \vec{A} rotating at the same angular velocity whose definition is given by:

$$\vec{A} = A_x \hat{x} + A_y \hat{y} + A_z \hat{z}\tag{63}$$

The time derivative of \vec{A} is given by:

$$\frac{d\vec{A}}{dt} = \frac{dA_x}{dt} \hat{x} + \frac{dA_y}{dt} \hat{y} + \frac{dA_z}{dt} \hat{z} + A_x \frac{d\hat{x}}{dt} + A_y \frac{d\hat{y}}{dt} + A_z \frac{d\hat{z}}{dt}\tag{64}$$

Using (35) this equation can be re-written as:

$$\frac{d\vec{A}}{dt} = \frac{dA_x}{dt} \hat{x} + \frac{dA_y}{dt} \hat{y} + \frac{dA_z}{dt} \hat{z} + \omega_{rf} \times \vec{A}\tag{65}$$

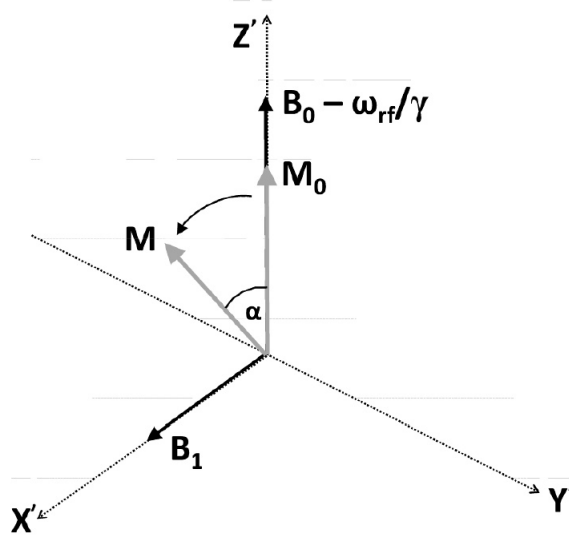


Figure 36: Precession of the bulk magnetization, \vec{M} , in the rotating frame of reference. When $\omega_{rf} = \omega_0$, the precession can be viewed simply as a tipping motion.

Which can be simplified further to

$$\frac{d\vec{A}}{dt} = \frac{\partial\vec{A}}{\partial t} + \omega_{rf} \times \vec{A} \quad (66)$$

where $\partial\vec{A}/\partial t$ is the rate of change of \vec{A} as observed in the rotating coordinate system. The equation of motion of the bulk magnetization in the rotating frame of reference can therefore be written as:

$$\frac{\partial\vec{M}}{\partial t} = \gamma\vec{M} \times \vec{B}_{eff} \quad (67)$$

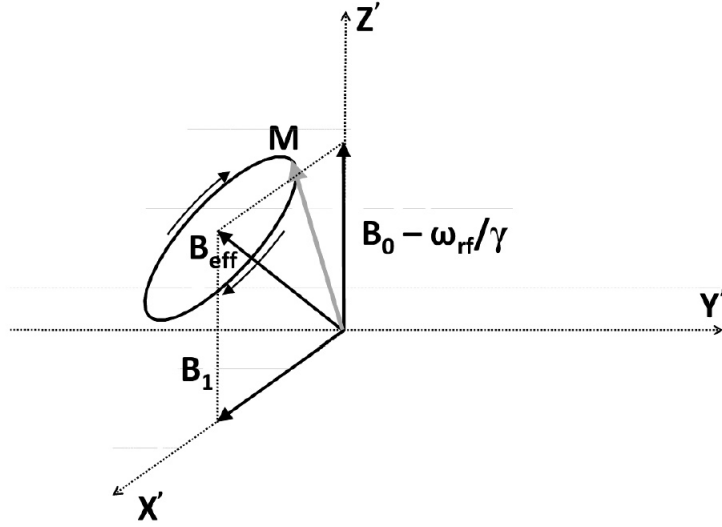


Figure 37: recession of the bulk magnetization, \vec{M} , in the rotating frame of reference. When $\omega_{rf} \neq \omega_0$, precession occurs about \vec{B}_{eff} .

where

$$\vec{B}_{eff} = \vec{B}_1 \hat{x} + \left(\vec{B}_0 - \frac{\omega_{rf}}{\gamma} \right) \quad (68)$$

Equations (39) and (40) show that the effective field, \vec{B}_{eff} , affects the bulk magnetization and is composed of the \vec{B}_0 field plus a fictitious field (ω_{rf}/γ) which is generated by the rotation of the rotating frame. If $\omega_{rf} = \omega_0$ then B_{eff} will be equal to \vec{B}_1 and there will be no effective field along the z' -axis meaning there will be no precession in the rotating frame this is shown in Figure 36. When $\omega_{rf} \neq \omega_0$ the \vec{B}_1 field being off resonance and the bulk

magnetization will precess about \vec{B}_{eff} as illustrated in Figure 37.

B The Flip Angle

As a result of applying an RF excitation field in the rotating frame, the bulk magnetization will tilt away from the z' -axis to the $x'y'$ plane at an angle α . This is known as the flip angle and is given by:

$$\alpha = \gamma \int_0^\tau B_1^e dt \quad (69)$$

where τ is the duration of the pulse. The pulse envelope function B_1^e is commonly referred to as the RF pulse itself. This is because the initial phase angle, ϕ , is kept constant as is the excitation frequency, ω_{rf} , which is determined by the resonance condition meaning both of these parameters have no significant effect on the excitation profile of the RF pulse. Indeed, the excitation profile of the RF pulse can be fully characterized by taking the Fourier transform of B_1^e using Fourier analysis.

If the envelope of the RF pulse is rectangular then the flip angle is given by:

$$\alpha = \gamma B_1 \tau \quad (70)$$

When the duration of the RF pulse is chosen to be $\tau = \pi/2\gamma B_1$ then the bulk magnetization is tilted 90° which generates maximum transverse mag-

netization. This is called a 90° pulse, Should the pulse duration be longer such that $\tau = \pi/\gamma B_1$ then the bulk magnetization is tilted 180° and said to be inverted. This is known as a 180° pulse.

While the shape of the duration of the pulse envelope determines the excitation profile of the RF pulse, they are not important when considering the flip angle providing $\int_0^\tau B_1^e dt$ is kept constant. For different envelope functions such as the previously mentioned rectangular pulse and the popular Sinc pulse, the bulk magnetization will end up in the same location but will traverse a different trajectory during the excitation period.

Once the RF pulse is turned off, \vec{M} will start to realign with the z' -axis and return to its equilibrium value, M_0 , through the process of relaxation.

C Spin Relaxation

T_1 Relaxation - Spin Lattice Relaxation

The T_1 relaxation process starts to take effect after the RF excitation pulse has ended. It is a measure of the characteristic time it takes for the longitudinal component of the bulk magnetization, M_z , to realign itself with \vec{B}_0 returning itself to state M_0 . The rate of change of M_z as it relaxes to M_0 can be described by first order kinetics and is governed by the equation:

$$\frac{dM_z}{dt} = -\frac{M_z - M_0}{T_1} \quad (71)$$

This differential equation has the solution:

$$M_z(t) = M_0 + (M_z(0) - M_0)e^{-\left(\frac{t}{T_1}\right)} \quad (72)$$

where $M_z(0)$ is the value of M_z at $t = 0$, or immediately after \vec{B}_1 is turned off. At $t = T_1$, 63% of the longitudinal magnetization is recovered and after $5T_1$ the sample is considered to be back to M_0 as shown in Figure 38.

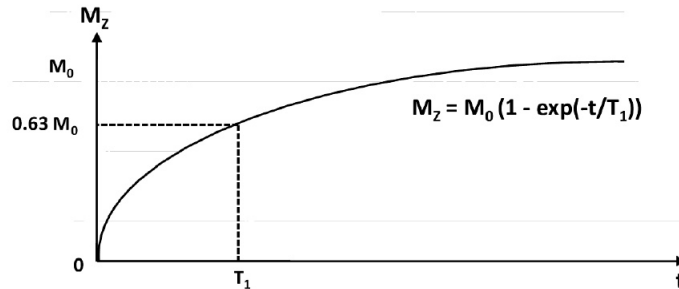


Figure 38: T_1 relaxation. At $t = T_1$, 63% of M_z has been recovered.

Spin lattice relaxation is typically induced by magnetic field fluctuations resulting from atomic or molecular motion which serve to transfer energy from the excited spin system to its environment (the 'lattice'). Specifically, this energy exchange occurs due to protons encountering a magnetic field which is fluctuating at the Larmor frequency. The source of this fluctuating field is a proton (or electron) attached to a molecule that is rotating at a rate which is similar to the Larmor frequency.

The molecular motion is characterized by the correlation time, τ_C , with such interactions being referred to as dipole-dipole interactions involving

energy exchange are more efficient resulting in shorter T_1 values. Small molecules such as H_2O have short correlation times (faster molecular rotation) and are therefore ineffective at T_1 relaxation. The T_1 of pure water is thus the longer in-vivo. The protons of Hydrogen nuclei in large macromolecules have long correlation times and also have long T_1 values. With H_2O molecules which are transiently bound to proteins and other macromolecules, the correlation times are much closer to $1/\omega_0$ resulting in shorter T_1 values. Free lipid molecules which are larger in size than water molecules also have shorter T_1 values. In general, the T_1 time increases with increased water content and decreases with increased molecular content.

It can be seen that T_1 is dependant on \vec{B}_0 . By increasing the field strength then ω_0 increases and dipole-dipole interactions become more probable for molecules with shorter correlation times.

T_2 Relaxation - Spin Spin Relaxation

When \vec{M} relaxes towards its equilibrium state M_0 , the transverse component of \vec{M} must decay to zero. Spin-spin relaxation is the measure of the timescale for transverse magnetization to persist in a uniform \vec{B}_0 field. However, due to local inhomogeneities in the \vec{B}_0 field, together with energy exchange between magnetic moments within the spin system (spin-spin interactions), phase coherence in the transverse plane will gradually be destroyed.

Loss of phase coherence occurs when protons experience a change in their local magnetic field due to interactions with neighbouring protons. The amount of interaction is once again dependant on the correlation time.

Molecules with long correlation times (slow molecular rotation) produce larger static fields causing greater dephasing which results in efficient T_2 relaxation and thus short T_2 values. Free water molecules have short correlation times hence have long T_2 values. In tissue, T_2 increases with increasing water content and decreases with increasing macromolecular content.

The T_2 relaxation time reflects both spin-lattice and spin-spin interactions and so is always less than or equal to T_1 . Unlike T_1 , T_2 is not susceptible to \vec{B}_0 since it is primarily caused by local field imperfections.

The rate of change of transverse magnetization is given by:

$$\begin{aligned}\frac{dM_x}{dt} &= -\frac{M_x}{T_2} \\ \frac{dM_y}{dt} &= -\frac{M_y}{T_2}\end{aligned}\tag{73}$$

where M_x and M_y are the components of the magnetization along the x and y axis in the rotating frame of reference. These equations have the solutions:

$$M_x(t) = M_x(0)e^{-\frac{t}{T_2}} \quad M_y(t) = M_y(0)e^{-\frac{t}{T_2}}\tag{74}$$

where $M_x(0)$ and $M_y(0)$ are the values of M_x and M_y at $t = 0$, immediately after \vec{B}_1 is switched off. The elapsed time between the maximum transverse magnetization and 37% of its value is the T_2 decay constant shown in Figure

39.

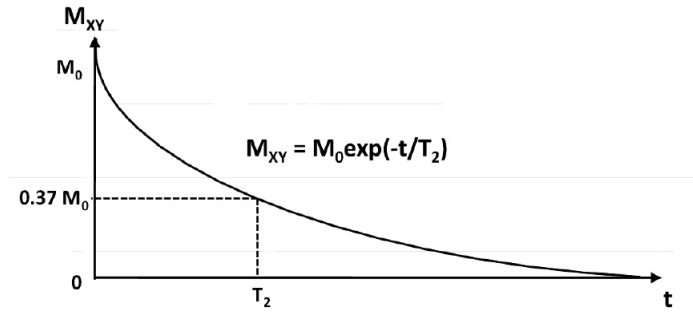


Figure 39: T_2 relaxation. At $t = T_2$, M_{xy} has decayed to 37% of its maximum value.

T_2^* Relaxation - Pseudo Relaxation

Pseudo relaxation is another method that contributes to the relaxation phenomenon. The T_2 relaxation process due to spin-spin interactions is a random process and is therefore irreversible. The faster T_2^* decay process is primarily due to an additional loss of phase coherence caused by inhomogeneities in the \vec{B}_0 field. These inhomogeneities may be attributed to intrinsic defects in the \vec{B}_0 field or may be caused by magnetic susceptibility effects from tissue or other materials placed in the field. Since these inhomogeneities are generally fixed in time and space then, this additional loss of phase coherence is reversible.

The time constant T_2^* is related to T_2 by the equation:

$$\frac{1}{T_2^*} = \frac{1}{T_2} + \frac{1}{T_{2SUS}} + \frac{1}{T_{2INH}} + \frac{1}{T_{2OTHER}} \quad (75)$$

where T_{2SUS} , T_{2INH} , and T_{2OTHER} are the transverse magnetization relaxation constants due to inhomogeneities in the magnetic field, local differences in susceptibility and magnetization, and other processes.

D RC Network

In order to minimize the induced voltage due to direct \vec{B}_1 exposure, a variety of filters were used to condition the signal for analysis. The use of an RC network to form a low-pass filter / integrator is used in conjunction with the half-wave diode rectifier to form an AM demodulator. A low pass filter allows low frequency signals from 0Hz to its cut-off frequency, f_c , to pass while blocking higher frequencies. The most common form of low-pass filter consists of a resistor in parallel with a load and a capacitor in parallel with the load. The capacitor's reactance is high at low frequencies thus forcing the signal through the load, whereas at high frequencies the capacitor functions as a short. The cutoff frequency of the filter f_c is determined by the time constant $\tau = RC$,

$$f_c = \frac{1}{2\pi RC} \quad (76)$$

For the purpose of this work, the high frequency which we wish to attenuate is 127.74MHz, with the low-frequency signal of interest being 575Hz.

In the use of an AM diode demodulator the low pass filter is required to remove the high frequency elements that remain within the signal after

detection / modulation. The RC filter can be used as an integrator for certain RC values. The RC time constant, τ , of the filter is critical in its effectiveness as it reflects the time required for the capacitor to charge up to 63.2% of the maximum voltage or to discharge down to 36.8% of its maximum voltage. By designing a filter which is too slow to transmit 128MHz signal, but fast enough to integrate the 578Hz signal, the combination of the diode rectifier and RC integrator can be utilized to demodulate Rabi oscillation.

E High-Pass Filter

Similar to the previously discussed low-pass filter, the high-pass filter most commonly consists of a capacitor in series with a resistor placed across the load. The filter blocks input signals up until the cut-off frequency is reached. Above this frequency the reactance of the capacitor has reduced such that it acts as a short and allowing the input to pass directly to the output.

F Half-Wave Diode Rectifier

A rectifier is simply the use of a diode converting alternating current (AC) into direct current (DC). The diode allows the flow of current in only one direction and blocks current in the other direction, using this allows for only the half cycle of the input signal to be transmitted through (Figure 40). When a half wave rectifier is used for amplitude modulation detection, the

circuit requires to interface to the other circuits in the

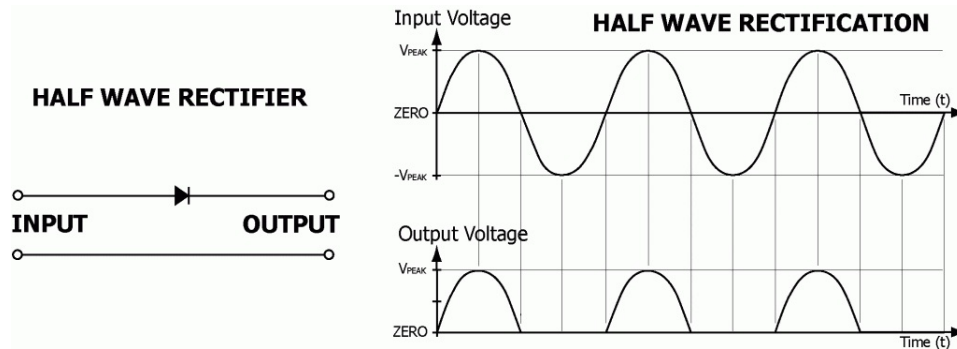
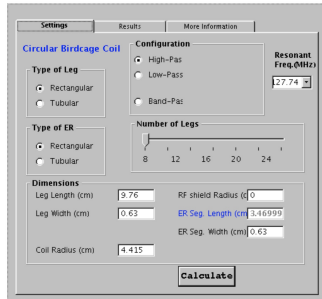


Figure 40: Half-Wave Diode Rectifier. The use of the diode allows for only half the input waveform to be passed through.

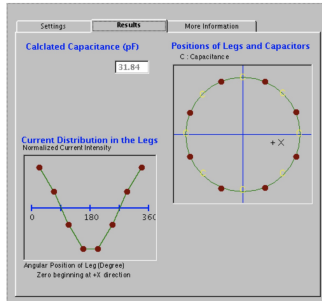
When a half wave rectifier is used for amplitude modulation detection it provides an output of the envelope of the signal. The diode detector consists of two main elements, the diode / rectifier as discussed and a low-pass filter.

G Birdcage Builder

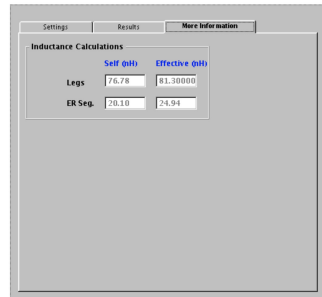
Birdcage builder is a software package that has been widely used all over the world in the field of MRI. It calculates the mutual inductance, effective inductance and capacitance values of an RF coil. [16] In this thesis birdcage builder software was used to for calculating the capacitance values based on the geometry of the coil (Figure 41).



(a)



(b)



(c)

Figure 41: (a) Coil specifications are defined to build a birdcage coil. (b) Calculated capacitance and position of the capacitors to be placed on the end ring. (c) Calculated self-inductance and effective inductance of the coil.

H Resonance Circuit Q Corrections to Induced Voltage

The LC resonant circuit was designed to have a resonance centered in the mid 500 Hz region. However, because of coil copper wire resistance in the tank primarily, the responsivity of the circuit is broadened enough in frequency to detect the lower 288Hz and higher 1150Hz Rabi signals. To correct for the Q variation however, one must determine the response curve. This was accomplished by scanning a sine wave frequency across the tank circuit (Figure 42) below using the LTSpice simulator for the circuit values used. The percentage of peak voltage in Figure 43 at 287.5Hz and 1150Hz were found to be 81.3% and 50.6% respectively.

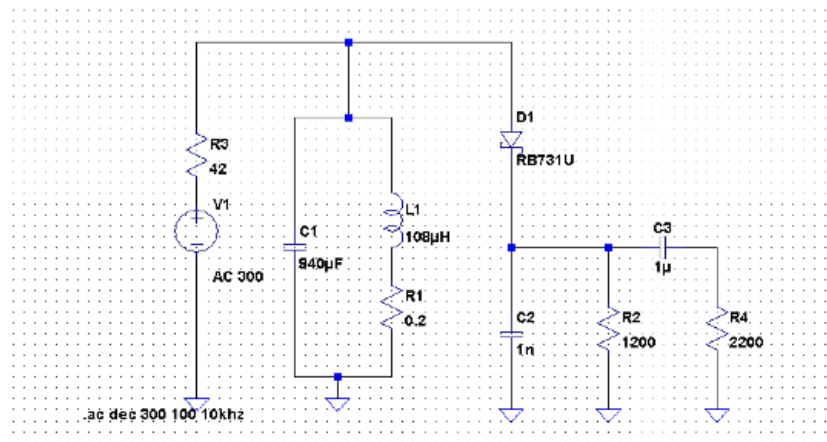


Figure 42: Circuit used in simulator for determining the quality Q of the frequency response.

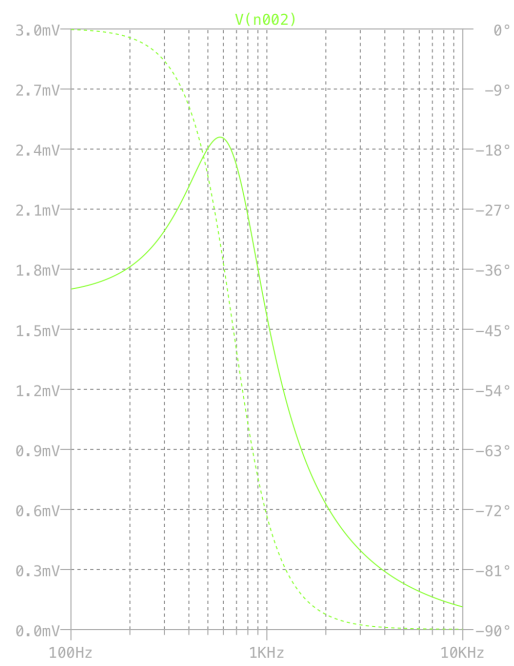


Figure 43: Voltage response of the circuit in Figure 42 as a function of frequency.